

Solid-state optical interconnect between distant superconducting quantum chipsKeyu Xia^{*} and Jason Twamley[†]*ARC Centre for Engineered Quantum Systems, Department of Physics and Astronomy, Macquarie University, NSW 2109, Australia*

(Received 25 August 2014; published 8 April 2015)

We propose a design for a quantum microwave-optical photonic interface using electron spins in crystals to adiabatically swap the quantum states between a flux qubit and optical cavity that can achieve a transfer fidelity in excess of 90%. Following detailed modeling, we show that our protocol is robust against inhomogeneous broadening of the microwave and optical transitions, phase mismatch between the microwave and optical fields, and has the advantage that we can dynamically control the overall microwave-optical coupling strength in time. Using these capabilities we show how to coherently transport quantum information between two distant superconducting chips optically with a fidelity exceeding 90%.

DOI: [10.1103/PhysRevA.91.042307](https://doi.org/10.1103/PhysRevA.91.042307)

PACS number(s): 03.67.Lx, 85.25.Am, 03.67.Hk, 42.50.Ct

I. INTRODUCTION

Superconducting qubits (SQs) are one of the most promising technologies for delivering a quantum computer which will operate within a single superconducting chip [1]. Linking remotely distant quantum systems, other than superconducting systems, e.g., atoms or ions, via an optical data bus has enjoyed some progress, but the technical challenges are considerable [2–4]. Here, we propose a scheme based on solid-state spins in crystals for microwave-to-optical (MW-O) quantum interface and with this to fashion a quantum network for SQs. In particular, we develop a scheme to controllably couple a superconducting flux qubit and an optical cavity via the crystal spins. Following detailed modeling, we show that our scheme can successfully address two of the main difficulties faced when controlling quantum dynamics in condensed-matter systems: (a) we can overcome significant levels of microwave and optical inhomogeneous broadening, (b) we can achieve high-coupling strengths while circumventing the phase mismatch that can build up between microwave and optical light fields in the crystal due to the enormous difference in wavelength.

Although the strong coupling between solid-state electronic spin ensembles and superconducting circuits has been experimentally demonstrated [5–8], these have been constrained to the interaction between microwave photons and electron or nuclear spins and none have explored how to couple to optical light fields. The latter are quite difficult due to their vast difference in frequencies but also the difference in coupling strengths between microwave and optical photons to spin ensembles. Recently, two proposals for a solid-state hybrid quantum interface have been proposed [9,10], but both propose very different physical setups than ours. The first work exploits a large crystal sample to enhance the magnetic coupling as the mode volume of the microwave resonator is extremely large. Such a large interaction region may suffer from detrimental phase mismatching between the microwave and optical cavity modes (not incorporated in the model), which may destroy the transfer. In addition, the microwave-ensemble coupling strength could be reduced when taking into account the

larger detunings required for the adiabatic elimination of the collectively coupled spin ensemble as compared to those required for an individual spin [11]. The work [10] involves the application of time- and position-dependent large magnetic fields over a large portion of a superconducting circuit in addition to a complex process: absorbing a single-photon pulse in the spin ensemble, then five staggered π pulses on resonance. This involves putting the spin ensemble into an optical excited state, but the effects of decay from this state on the transfer efficiency are not obvious (not included in the model), and no inhomogeneity in this optical transition is discussed, only in the magnetic transition. Due to the unknown optical and microwave inhomogeneous broadening (sometimes considerable) in condensed state matter, which can lead to enormous rates of decay into dark states [12], it is practically impossible to effect perfect π pulses [13]. Our design addresses all of these issues and further, one has complete temporal control over the overall microwave-optical coupling strength, allowing complex protocols to be built.

II. SYSTEM AND MODEL

We begin by describing the schematic configuration for our quantum interface or node and later how to use two distant nodes to achieve quantum state transfer, i.e., a quantum network (Fig. 1). Each node works as a quantum interface and composes of a Fabry-Pérot cavity, an ensemble of spins, and a gap-tunable four-Josephson-junction (4JJ) flux qubit. This 4JJ flux qubit is fabricated on top of a suitable substrate (dark plane) (Fig. 1). In order to optically couple the ensemble of spins in a crystal chip, a round hole is cut in the main loop of the flux qubit such that the light in the Fabry-Pérot cavity can pass through it without significant absorption and scattering. The crystal chip covers the hole. In this arrangement, the spin ensemble can effectively couple to both of the cavity mode and the magnetic field created by the flux qubit (see Appendix for more details). We consider that an optical coherent control field irradiates the crystal chip at almost normal incidence to the chip.

We now describe the optical subsystem of each node and the unidirectional optical fiber couplings [14,15]. We assume that the optical cavity mode $\hat{a}_{c,l}$ in the l th node ($l \in \{A, B\}$) has a resonance frequency $\omega_{c,l}$ and an intrinsic decay rate $\kappa_l^{(l)}$.

^{*}keyu.xia@mq.edu.au[†]jason.twamley@mq.edu.au

It couples to an output optical fiber with a coupling rate $\kappa_{ex}^{(l)}$ and connects to the other node via this fiber. Thus, the total decay rate becomes $\kappa_l = \kappa_i^{(l)} + \kappa_{ex}^{(l)}$, and we assume $\kappa_{ex}^{(l)} = \xi_l \kappa_l$ with $0 \leq \xi_l \leq 1$. $\xi_l < 1$ represents the photon loss in the transfer. In this two-node network, the Lindblad superoperator describing the one-way quantum connection breaking the time symmetry is given by $\hat{L}_{net} = -\sqrt{\kappa_{ex,A}\kappa_{ex,B}}(\hat{a}_B^\dagger \hat{a}_A \rho - \hat{a}_A \rho \hat{a}_B^\dagger + \rho \hat{a}_A^\dagger \hat{a}_B - \hat{a}_B \rho \hat{a}_A^\dagger)$, where \hat{a}_A^\dagger (\hat{a}_B^\dagger) and \hat{a}_A (\hat{a}_B) are the creation and annihilation operators of the cavity mode in node A (B).

We next describe the crystal-chip spin ensemble. We model the collection of electron spins as ensemble of three-level systems, as shown in Fig. 1(b). These could be either a collection of NV⁻ centers in diamond [16] or rare-earth ion crystal such as Er³⁺ ions in Y₂SiO₅ [17,18]. Each spin system consists of three levels: the optical excited state $|r_j\rangle$, and two electronic ground states $|g_j\rangle$ and $|e_j\rangle$. In the case of the NV⁻ we have $\{|r_j\rangle, |g_j\rangle, |e_j\rangle\} = \{|^3E, S_z\rangle_j, |^3A, m_s = 0\rangle_j, (|^3A, m_s = +1\rangle_j + |^3A, m_s = -1\rangle_j)/\sqrt{2}\rangle_j\}$, while for the Er³⁺ system we have $\{|r_j\rangle, |g_j\rangle, |e_j\rangle\} = \{|^4I_{13/2}, Y_1\rangle_j, |^4I_{15/2}, Z_1, m_s = -1/2\rangle_j, |^4I_{15/2}, Z_1, m_s = +1/2\rangle_j\}$. The excited state $|r_j\rangle$ decays to the state $|g_j\rangle$ ($|e_j\rangle$) with a rate $\gamma_{0,j}$ ($\gamma_{1,j}$). Due to the coupling to the magnetic environment, the state $|e_j\rangle$ also decays to $|g_j\rangle$ with the rate $\Gamma_{1,j}$ and suffers pure dephasing of a rate $\Gamma_{\phi,j}$. We can describe the ensemble of spins within each node with the Hamiltonian ($\hbar = 1$)

$$H_{\text{spin}} = \sum_j \frac{D_j}{2} S_{z,j} + g_e \mu_B \mathbf{B}_{z,j} \cdot \mathbf{S}_{z,j} + \omega_{r,j} |r_j\rangle \langle r_j|, \quad (1)$$

where $S_{z,j}$ is the z component of the usual spin- $\frac{1}{2}$ Pauli operators \mathbf{S}_j for the j th spin, D_j is the zero-field splitting with $D_j \approx 2.8$ GHz (4 GHz) for the NV⁻ (Er³⁺) centers, $\omega_{r,j}$ is the energy of the optical excited state $|r_j\rangle$. The second term describes the magnetic interaction with the spins with g_e being the Landé g factor of the spin and $\mu_B = 14$ MHzmT⁻¹ is the Bohr magneton. Note that rare-earth ions are preferable for a large magnetic coupling because the g factor of the electronic

spin in Er³⁺ can be up to $g_e \sim 15$, which is much larger than in NV⁻ centers where $g_e \sim 2$. Here, we neglect the terms related to the strain-induced splitting because they are very small and only shift the energy of state $|e_j\rangle$.

The 4JJ flux qubit can be modeled as a two-level system with the excited state $|e_f\rangle$ and the ground state $|g_f\rangle$, and can be tuned by the flux biases Φ_b and Φ_a . The flux Φ_a threading through the α loop is used to tune the gap $\mathcal{T}(\Phi_a)$. We apply a time-dependent magnetic field $\Phi_\mu(t) = A_\mu(t) \cos(\omega_\mu t)$ to the α loop and thus tune the gap of qubit. Thus, the free Hamiltonian of the gap-tunable flux qubit becomes $H_Q = \omega_q/2 \sigma_z + \Omega_\mu \cos(\omega_\mu t) \sigma_z$, where $\omega_q = \sqrt{\mathcal{T}^2 + \epsilon^2}$ with $\epsilon(\Phi_b) = 2I_p(\Phi_b - \Phi_0/2)$ (Φ_b is the external flux threading the qubit loop, Φ_0 the flux quantum, and I_p the persistent current) the energy bias and \mathcal{T} is the tunnel splitting dependent on the bias Φ_a , and $\Omega_\mu \propto A_\mu$. In the vicinity of $\Phi_b \approx \Phi_0/2$ we have $\mathcal{T}(\Phi_a) \gg \epsilon$. The flux qubit associated Pauli spin- $\frac{1}{2}$ operators is defined as $\sigma_z = |e_f\rangle \langle e_f| - |g_f\rangle \langle g_f|$ and $\sigma_x = |e_f\rangle \langle g_f| + |g_f\rangle \langle e_f|$. The decay and pure dephasing rates of the excited state of the flux qubit $|e_f\rangle$ are denoted as $\gamma_{1,qb}$ and $\gamma_{2,qb}^*$, respectively.

We now describe the tripartite interaction between the ensemble of spins, the cavity mode, and the flux qubit within an individual node shown by Fig. 1(b). We consider an optical Raman transition between the two spin ground states $|g_j\rangle$ and $|e_j\rangle$ formed through a combination of the external driving classical optical field and the quantum optical cavity field. This optical driving of an individual spin at position \mathbf{R}_j together with the cavity mode $\hat{a}_{c,j}$ drives the transition of $|g_j\rangle \leftrightarrow |r_j\rangle$ with a rate $g_{c,j}$ and a phase θ_j dependent on the position \mathbf{R}_j and the wave vector \mathbf{k} of $\hat{a}_{c,j}$. The coherent laser field $\Omega_{c,j}$, with the frequency ω_L and chirped phase $\phi(t)$, drives the transition of $|e_j\rangle \leftrightarrow |r_j\rangle$. The fluctuation in the coherent driving is taken into account by θ_j and $g_{c,j}$. In the dispersive regime, these optical transitions form a Raman transition between the two ground states $|g_j\rangle$ and $|e_j\rangle$, which is also arranged to dispersively couple to the flux qubit. Such optical Λ -type configuration has been demonstrated in both ensembles of NV⁻ centers [16] and Er³⁺ host crystals [17,19,20]. The total

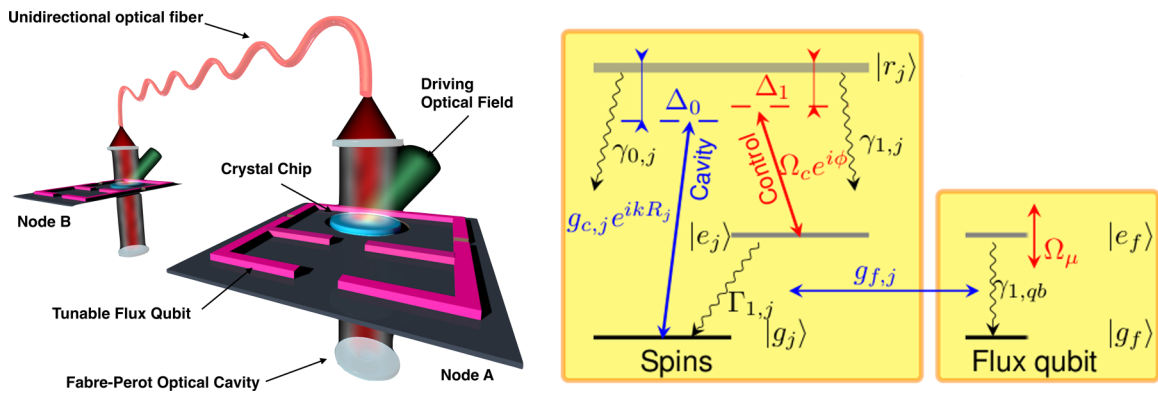


FIG. 1. (Color online) Schematic design and operation of the quantum network. (a) Schematic of quantum network between two superconducting flux qubits. Nodes A and B are identical and connected by a one-way optical fiber. Each node consists of a four-junction flux qubit and an ensemble of electronic spins. (b) Level diagram describing the interactions between the j th spin and the flux qubit and the optical cavity mode. Each spin is modeled as a Λ -type three-level system, while the gap-tunable flux qubit is modeled as a two-level system. The coherent (cavity) optical field $\Omega_c(\hat{a}_c)$ drives the transition $|r_j\rangle \rightarrow |e_j\rangle(|g_j\rangle)$. The flux qubit magnetically drives the transition $|e_j\rangle \rightarrow |g_j\rangle$.

Hamiltonian of the coupled system within one node is

$$\begin{aligned}
 H = & \frac{\omega_q}{2} \sigma_z + \Omega_\mu \cos(\omega_\mu t) \sigma_z + \sum_j^N g_{f,j} \sigma_x S_{x,j} \\
 & + \sum_j^N \frac{D_j}{2} S_{z,j} + \omega_{r,j} |r_j\rangle \langle r_j| + \omega_c \hat{a}^\dagger \hat{a} \\
 & + \sum_j^N (g_{c,j} e^{ikR_j} \hat{a}^\dagger |g_j\rangle \langle r_j| + \text{H.c.}) \\
 & + \sum_j^N \Omega_c (e^{i\omega_L t + i\phi(t)} |e_j\rangle \langle r_j| + \text{H.c.}). \quad (2)
 \end{aligned}$$

We consider the first-order sideband transition and adiabatically eliminate the optical excited state $|r_j\rangle$, then the Hamiltonian in the one-excitation space (OES) becomes (see Appendix)

$$\begin{aligned}
 H = & (\dot{\phi} + \tilde{\Delta}_q) \sigma_+ \sigma_- - \sum_j^N \Delta_j \tilde{S}_{+,j} \tilde{S}_{-,j} - \delta_{en} \hat{a}^\dagger \hat{a} \\
 & - \sum_j^N \left[g_{f,j} J_1 \left(\frac{\Omega_\mu}{\omega_\mu} \right) \tilde{S}_{+,j} \sigma_- + \Lambda_j \xi_j e^{i\theta_j} \hat{a}^\dagger \tilde{S}_{-,j} + \text{H.c.} \right],
 \end{aligned}$$

where $\dot{\phi}$ is the chirp of the coherent driving. Here, we define the detuning $\Delta_j = \omega_{r,j} - \omega_r$ with $\omega_r = \langle \omega_{r,j} \rangle$, $\delta = \omega_L - \omega_c$, $\Delta_0 = \omega_r - \omega_c$, and $\Delta_1 = (\omega_r - \omega_L) - \bar{D}$ with $\bar{D} = \langle D_j \rangle$, $\Delta_q = \omega_q - \delta$. $\langle \dots \rangle$ means the statistical ensemble average. We have the identity $\Delta_1 - \Delta_0 = \delta - \bar{D}$. Under the two-photon resonance condition, $\delta = \bar{D}$, and we also have $\tilde{\Delta}_q = \Delta_q - \omega_\mu$, $\delta_{en} = \sum_j^N \frac{g_{c,j}^2}{\Delta_0 + \Delta_j}$, $\Delta_{\text{spin},j} = [\Delta_1 - \Delta_0 - \delta_j - \dot{\phi} + \frac{\Omega_c^2}{\Delta_1 + \Delta_j - \delta_j}]$, and we define the operators $\tilde{S}_{+,j} = |e_j\rangle \langle g_j|$ and $\tilde{S}_{-,j} = \tilde{S}_{+,j}^\dagger$, while $J_1(x)$ is the Bessel function of the first kind. Here, we assume that $|\Delta_0|, |\Delta_1| \gg \gamma_j$ with $\gamma_j = \gamma_{0,j} + \gamma_{1,j}$, and set $\Lambda_j = \frac{\Omega_c}{2} \bar{g}_c \left(\frac{1}{\Delta_0 + \Delta_j} + \frac{1}{\Delta_1 + \Delta_j - \delta_j} \right)$, and $\xi_j = \frac{g_{c,j}}{\bar{g}_c}$, with $\bar{g}_c = \langle g_{c,j} \rangle$. Note that the detuning δ_{en} and the parameters $g_{f,j}, \xi_j, \theta_j$ are fixed once the setup is fabricated. A major advantage of our sideband transition configuration is that it allows one to modulate the coupling rate within the tripartite configuration of flux-spin ensemble-optical mode. This flexibility will later permit us to use stimulated Raman adiabatic passage (STIRAP) for quantum transfer and this has tremendous advantage as regards robustness to noise and parameter imprecision over fixed on-resonance coupling schemes for transfer [8,12].

III. NUMERICAL RESULTS

We can now consider the swap of quantum information between the flux qubit and the optical cavity mode in one interface. We first determine a good model for the spin ensemble with inhomogeneous broadening in the transition frequencies and coupling rates. We divide the spins into $N_g = 20$ groups and consider small inhomogeneities between the groups for the coupling rates $g_{c,j}$, and transitions frequencies D_j and $\omega_{r,j}$. This model reproduces quite precisely the Rabi

oscillations observed in the experimental observation [8], and we use this model for our numerical investigations following. Correspondingly, the Jaynes-Cummings coupling rates $g_{f,j}$, and $g_{c,j}$ are the cooperative coupling rates of the j th group which is increased by a factor $\sqrt{N_j}$ with respect to the single-spin coupling rate. Unlike the quantum memory by Zhu *et al.* [8], the strength of the overall magnetic coupling rate between the spin ensemble and the flux qubit is limited by the applicable thickness of the crystal chip hosting the spins. We will find that crystal chip must be quite thin to avoid degradation of the transfer fidelity due to phase mismatching and this reduced thickness restricts the degree of achievable magnetic coupling.

To swap quantum information from the flux qubit to the cavity mode we perform a two-photon resonant STIRAP transfer of the population from the flux qubit to the optical cavity, shown in Fig. 2. The system is initially populated in the excited state of the flux qubit $\langle \sigma_{ee}(t=0) \rangle = 1$. We modulate the coherent optical driving Ω_c and the flux bias Ω_μ such that two Rabi frequencies are Gaussian functions given by $J_1[\Omega_\mu(t)/\omega_\mu] = 0.58e^{-(t-\tau_{d,f})^2/2\tau_f^2}$ and $\Omega_c(t) = \Omega_{c,0}e^{-(t-\tau_{d,c})^2/2\tau_c^2}$ with the amplitude $\Omega_{c,0}$ of the coherent classical optical control field. To minimize the operation time, the three subsystems interact on resonance such that $\dot{\phi} = \Delta_1 - \Delta_0 + \Omega_c^2/\Delta_1 - \delta_{en}$ and $\dot{\phi} + \tilde{\Delta}_q = -\delta_{en}$, yielding $\omega_\mu = \Delta_q + (\Delta_1 - \Delta_0) + \Omega_c^2/\Delta_1$. For $\Omega_{c,0}/\kappa, \langle g_{f,j} \rangle/\kappa \gg 1$, we can finish the swap operation before the loss of the excitation due to any decay within the system. Here, $0.58\sqrt{N}\langle g_{f,j} \rangle \approx \Lambda_j \approx 105$ MHz. An advantage of this STIRAP transfer is that the excitation of the spins is greatly suppressed. As a result, the detrimental effect of the inhomogeneous broadening of the spins is very small.

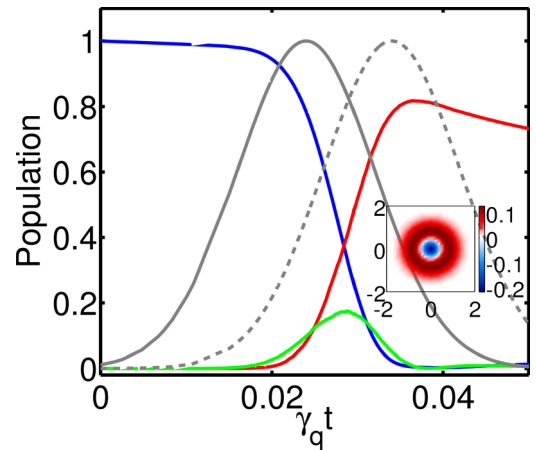


FIG. 2. (Color online) Swap of quantum information from the flux qubit to the cavity mode via the STIRAP protocol. Gray lines are the time-modulated STIRAP couplings via a driving classical optical field $\Omega_c(t)$ (solid line) and modulated cavity-QED coupling strength $g_f J_1[\Omega_\mu(t)/\omega_\mu]$ (dashed line). Blue line shows the population of the excited state of the source flux qubit, red line is the population of the target photonic state $|n=1\rangle$, while green line shows collective excitation of the spins. Inset is the Wigner function of the cavity mode at $\gamma_{1,qb}t = 0.036$. Other parameters are $\gamma_{1,qb} = 0.4$ MHz, $\kappa = 3$ MHz, and $g = 105$ MHz.

Figure 2 shows how well our STIRAP-based swap scheme works for $\gamma_{1,qb} = 0.4$ MHz, $\kappa = 3$ MHz. Such high-quality flux qubits [21,22] and Fabry-Pérot cavities [23] are available using existing experimental technology. To perform the STIRAP control, the pulse $J_1[\Omega_\mu(t)/\omega_\mu]$ follows the pulse $\Omega_c(t)$ with a delay $\tau_{d,f} - \tau_{d,c} = 1.25\tau_f$ and $\tau_f = \tau_c = 3$ ns ($0.008\gamma_{1,qb}^{-1}$, see Appendix). At $\gamma_{1,qb}t = 0.036$, the fidelity of the photonic state $|n=1\rangle$ reaches its maximum $\mathcal{F} = \sqrt{\langle\Psi|\rho|\Psi\rangle} = 0.904$ corresponding to a population of $P_{|n=1\rangle} = 0.817$. For $\gamma_{1,qb} = 0.4$ MHz, we can achieve a swap fidelity larger than 0.81 if $\kappa \leq 5\gamma_{1,qb}$ and $g > 40$ MHz. A simpler implementation of the STIRAP technology using a constant chip corresponding to the maximal ac Stark shift $\Omega_{c,0}^2/\Delta_1$ can still reach $\mathcal{F} = 0.897$ at $\gamma_{1,qb}t = 0.035$.

Now, we use our microwave-optical quantum interface to transfer quantum information between two remote SQs by exploiting the scheme proposed by Cirac *et al.* [14], and to construct a quantum internet. To do so, we create a tripartite Raman transition where the spin ensemble dispersively couples to the flux qubits and the cavity modes with detuning $20\sqrt{N}g_f$. According to the scheme [14,24], we need only tune the coupling Λ_j by modulating the control field Ω_c and can set $\Omega_\mu = 0$. In the simulation, we eliminate the small time delay in the control field Ω_c of the node *B* related to the retardation in the propagation between two nodes [14]. As an example, Fig. 3 shows the distant transfer of the quantum state from node *A* to node *B*. We assume that two nodes are identical. The flux-qubit-spin ensemble coupling rates $\sqrt{N}g_{f,j} = 10\kappa$ with $\kappa = 10$ MHz is constant in time, while we modulate the optical Raman coupling via the classical laser driving field $\Omega_c = \Omega_{c,0} \text{sech}[-(t - \tau_{d,c})/\tau_c]$, with $\Omega_{c,0} = 200\kappa$ and $\Delta_0 = 20\Omega_{c,0}$. As a result, the excitation in the flux qubit in node *A* is transferred to the flux qubit in node *B* with a fidelity in excess of 90%. For NV^- centers, we use the collective decay rate of the ensemble of spins $\Gamma_{1,en} = 12$ MHz for fitting the experimental data. The quantum state of the flux qubit *A* can be transferred to qubit *B* with a fidelity of $\mathcal{F} = 93.3\%$ corresponding to a node *B* population of 0.87 at $\kappa t = 9.55$. While for the ensemble of Er^{3+} , the spin magnetic

excited-state decay can be neglected as $T_1 = 4$ s [25], and the inhomogeneous broadening is 13.8 MHz. This negligible decay increases the fidelity slightly to 95.1% (population of 0.904).

Next, we compare the available magnetic coupling rates in two implementations using NV^- centers or rare-earth ions. Both the swapping and remote transfer of the quantum information require a strong coupling between the flux qubit and the spins. However, the physical size of the spin ensemble is constrained by the area of the flux qubit and also the crystal chip must be quite thin to reduce the detrimental effects of optical phase mismatch on the transfer fidelity. Due to their large electron *g* factors [25], rare-earth ions such as Er^{3+} can provide a coupling rate of about 400 MHz, which is large enough for our task. However, the largest usable magnetic coupling strength between the flux qubit and the ensemble of NV^- centers is only about 19 MHz. To increase the coupling rate, we can focus the magnetic flux on the small diamond chip using superconducting flux focusing techniques [26–28], and utilizing this our scheme can be usefully applied to an ensemble of NV^- centers to achieve good transfer fidelities.

IV. CONCLUSION

In summary, we have proposed a theoretical scheme for an all-solid-state quantum interface between microwave and optical quantum information with sufficient tunability to permit local and long-distance high-fidelity quantum transfer. Our scheme uses a coupling configuration which incorporates either a combined Raman-STIRAP control or a three-body Raman control to robustly swap between the superconducting qubit and the optical cavity with full dynamical tunability of the transfer. Using this quantum interface, we have demonstrated the proof-in-principle quantum network transferring the quantum information with a fidelity larger than 90% between two remote superconducting qubits.

ACKNOWLEDGMENT

This work was partially funded by the Australian Research Council Centre of Excellence for Engineered Quantum Systems (EQUS), Project No. CE110001013.

APPENDIX

Our device for quantum interface and quantum network mainly includes three subsystems: a gap-tunable flux qubit, an ensemble of spins doped in a crystal chip, and optical cavities connected via an optical fiber.

To provide the readers a clear picture for the complicated protocol and simulation in the main paper, we include the detailed discussions about the implementation of our device, the model and method, the more specified level diagram in this Appendix.

In this appendix, we present a model to reproduce the experimental measurement by Zhu *et al.* [8]. We first model the gap-tunable flux qubit and then its interaction with an ensemble of spins in the one-excitation space. By fitting the experimental data, we justify our model valid and all parameters for the system reasonable. Then, we provide a detailed method

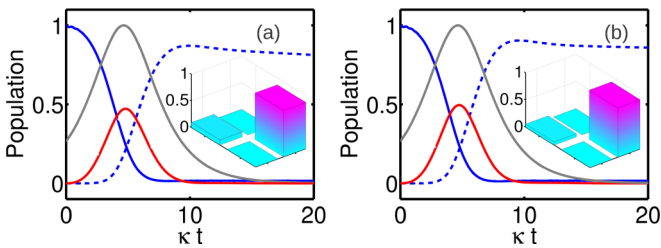


FIG. 3. (Color online) Transfer of quantum information between two distant flux qubits (a) using an ensemble of NV^- centers with $\Gamma_{1,en} = 12$ MHz, while (b) using an ensemble of Er^{3+} with $\Gamma_{1,en} \sim 0$. Solid (dashed) blue line graphs the excitation of the source qubit *A* (target qubit *B*), red line is the excitation of the antisymmetric state of the combined cavity modes of nodes *A* and *B*, while the gray line shows the control pulses (identical and simultaneous in both nodes). The inset shows the density matrix of the superconducting qubit at node *B* at $\kappa t \sim 10$. Other parameters are $\gamma_{1,qb} = 20$ kHz, $\gamma_{2,qb}^* = 0$, $\Gamma_{2,en}^* = 0.9$ MHz, $\sigma_\Delta = 14.4$ MHz, $\sigma_\theta = 0.1\pi$.

showing how a quantum interface interconverts the microwave quantum information to optical and how to swap the quantum state from the flux qubit to an added optical cavity. All simulations are performed in the so-called one-excitation space. In the end, we compare the two implementations using ensemble of NV centers and rare-earth ions.

1. Reproduction of experimental results

Before we study the swap and distant transfer of a quantum state, we present a model to reproduce the experimental observation by Zhu *et al.* [8]. Through this study, we are able to gain a sufficient detailed description of the NV diamond + flux qubit hybrid system to enable our further investigation into swap and distant transfer.

a. A gap-tunable flux qubit

Superconducting flux qubits consisting of three Josephson junctions (JJs) embedded in a low-inductance superconducting loop have shown to be promising candidates for quantum computing [29]. With the standard design, the magnetic flux (Φ_b) passing through the loop, which induces an energy difference ϵ between the ground state and the first excited state, is the only tunable parameter during the experiment. At the degeneracy point, namely, when $\Phi_b = (n + 1/2)\Phi_0$ (with integer n and the quantum flux Φ_0), the energy spacing reaches its minimum value, the so-called gap \mathcal{T} , which is related to the quantum mechanical tunnel rate. This degeneracy point is optimal because at this point the flux qubit is decoupled to the first order from low-frequency flux noise ($1/f$ noise) and has maximum coherence time [29]. Away from this sweet point, the decoherence time drops rapidly. In comparison with the standard three-JJ design, the gap of the four-JJ flux qubit replacing the smallest junction with a dc-SQUID can be tuned without leaving its optimal work point [8,22,30].

A gap-tunable flux qubit used in our scheme for quantum transfer is shown in Fig. 4. Two identical junctions with Josephson energy E_J in series with a symmetric dc-SQUID, in which each junction has Josephson energy of $\alpha_0 E_J$, are enclosed in a dc superconducting loop [8,22]. The control current I_2 created by the line 2 mainly generates the magnetic flux Φ_b threading the main loop (magenta loop) [22]. It is used to tune the energy difference $\epsilon = 2I_p[\Phi_b - (n + \frac{1}{2}\Phi_0)]$ with I_p the persistent current of the flux qubit through the main loop. To decouple the current I_1 from the main loop, our design use a sketched dc loop to increase the distance between the line 1 and the main loop, and subsequently decreases their mutual inductance. Thus, the flux Φ_α is only induced by the current I_1 in the control line 1. This arrangement has an advantage over the normal design by allowing one to separately tune the magnetic flux Φ_b and Φ_α via the control currents I_2 and I_1 , respectively. The dc-SQUID (green loop) works as an effective Josephson junction with energy of $\alpha E_J = 2\alpha_0 \cos(\pi \Phi_\alpha / \Phi_0) E_J$.

With the bias magnetic fluxes set as Φ_b and Φ_α , the flux qubit can be modeled as a two-level system with the original Hamiltonian ($\hbar = 1$) [22]

$$\hat{H} = \frac{\epsilon}{2} \sigma'_z + \frac{\mathcal{T}(\Phi_\alpha)}{2} \sigma'_x, \quad (\text{A1})$$

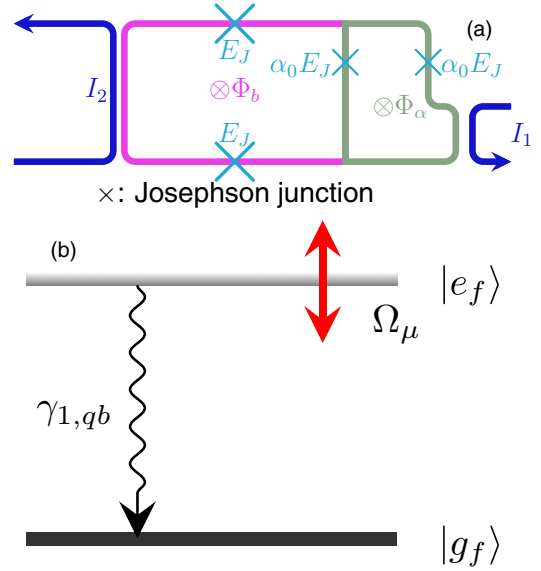


FIG. 4. (Color online) (a) Schematic diagram of a four-JJ flux qubit consisting of a main loop (magenta) and a dc-SQUID loop (green). The smallest Josephson junction is replaced by two identical Josephson junctions forming a dc-SQUID. (b) Level diagram of the four-JJ flux qubit modeled as a two-level system with the ground state $|g_f\rangle$ and the excited state $|e_f\rangle$. The main control current I_2 creates the magnetic flux threading the main loop and is used to tune the transition frequency, while the current I_1 is used to tune the tunneling between the two levels.

where the spin operators $\sigma'_z = |e'\rangle\langle e'| - |g'\rangle\langle g'|$ and $\sigma'_x = |e'\rangle\langle g'| + |g'\rangle\langle e'|$ with $|e'\rangle$ ($|g'\rangle$) the excited (ground) state of the flux qubit. $\mathcal{T}(\Phi_\alpha)$ is the tunnel rate between these two states and can be evaluated as $\mathcal{T}(\Phi_\alpha) = \omega_a/2\pi \exp\{-\sqrt{4\alpha(1+2\alpha)}E_J/E_c(\sin\phi_m^* - \frac{1}{2\alpha}\phi_m^*)\}$ through the WKB approximation according to the tight-binding model [29], where ω_a is the attempt frequency of escape in the potential well and $\cos\phi_m^* = 0.5\alpha$. For a general discussion, we assume that the flux qubit operates at the optimal point such that $\mathcal{T} \gg \epsilon$, and apply a time-dependent flux $\delta\Phi_\alpha(t)$ in Φ_α to create a tunnel element $\mathcal{T} = \mathcal{T}_0 + \Omega_\mu \cos(\omega_\mu t)$. Using the transform

$$|e_f\rangle = \cos(\theta/2)|e'_f\rangle + \sin(\theta/2)|g'_f\rangle, \quad (\text{A2})$$

$$|g_f\rangle = \sin(\theta/2)|e'_f\rangle - \cos(\theta/2)|g'_f\rangle \quad (\text{A3})$$

and

$$\sigma'_z = \cos\theta\sigma_z + \sin\theta\sigma_x, \quad (\text{A4})$$

$$\sigma'_x = \sin\theta\sigma_z - \cos\theta\sigma_x, \quad (\text{A5})$$

with $\sin\theta = \frac{\mathcal{T}}{\sqrt{\mathcal{T}^2 + \epsilon^2}}$ and $\cos\theta = \frac{\epsilon}{\sqrt{\mathcal{T}^2 + \epsilon^2}}$, we have the Hamiltonian

$$\hat{H}_0 = \frac{\omega_q}{2} \sigma_z + \Omega_\mu \cos(\omega_\mu t) \sigma_z \quad (\text{A6})$$

with $\omega_q = \sqrt{\mathcal{T}^2 + \epsilon^2}$ the transition frequency of the flux qubit in the basis of $\{|e_f\rangle, |g_f\rangle\}$. We model the flux-qubit dissipation

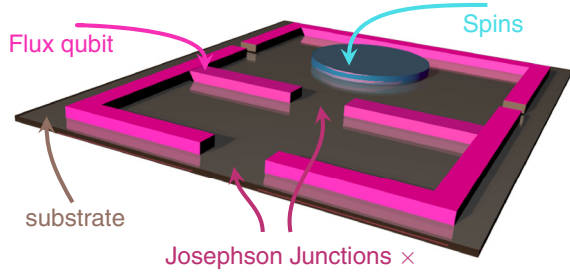


FIG. 5. (Color online) Schematic design of the chip coupling a flux qubit (magenta bars) to an ensemble of electron spins in a crystal chip (cyan cylinder). The gaps between the magenta bars denote the weak connections (Josephson junctions) of the flux qubits. The flux qubit and the crystal chip are fabricated on a substrate (gray base).

and the pure dephasing by

$$\mathcal{L}_q^{(1)} \rho = \frac{\gamma_{1,qb}}{2} (2\sigma_- \rho \sigma_+ - \sigma_+ \sigma_- \rho - \rho \sigma_+ \sigma_-), \quad (\text{A7})$$

$$\mathcal{L}_q^{(2)} \rho = \Gamma_{2,qb}^* (\sigma_z \rho \sigma_z - \rho), \quad (\text{A8})$$

where $\gamma_{1,qb}$ and $\Gamma_{2,qb}^*$ are the decay rate and the pure dephasing rate of the flux qubit, respectively. The flux qubit with a loop radius R_Q and a persistent current I_p can generate a quantum-state-dependent magnetic field

$$B \sim \frac{\mu_0 I_p}{2R_Q} \sigma_z. \quad (\text{A9})$$

b. Modeling of interaction between flux qubits and ensemble of NV^- centers

Now, we study the interaction between a flux qubit and an ensemble of NV^- centers. In the design shown in Fig. 5, the four-JJ flux qubit is made on top of a wafer. In the main loop of qubit, we make a hole through the wafer (to admit light) and the diamond crystal chip with a thickness of tens of nm covers the hole of the wafer. This design allows the NV^- centers to couple to an optical cavity mode later.

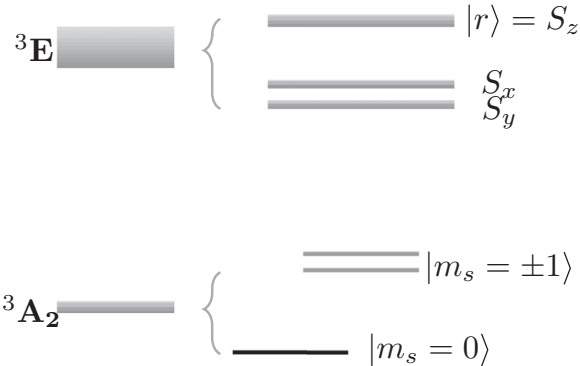


FIG. 6. Level diagram of a single NV^- center [31–34]. Both of the excited and ground states are triplet. The state $|r\rangle = |^3\text{E}, S_z\rangle$ can optically couple to the ground state $|^3\text{A}_2, m_s = 0\rangle$ and $|^3\text{A}_2, m_s = \pm 1\rangle$.

A single NV^- center in diamond can be modeled as in Fig. 6. The free Hamiltonian of NV^- centers is given by

$$\begin{aligned} H_{\text{NV}0} &= \sum_j^N D_j S_{z,j}^2 + E_j (S_{x,j}^2 - S_{y,j}^2) \\ &\quad + g_e \mu_B \mathbf{B}_j \cdot \mathbf{S}_j + \omega_{r,j} |r\rangle_j \langle r| \\ &= \sum_j^N D_j S_{z,j}^2 + E_j (S_{x,j}^2 - S_{y,j}^2) + g_e \mu_B B_{z,j} S_{z,j} \\ &\quad + g_e \mu_B B_{\perp,j} S_{\perp,j} + \omega_{r,j} |r\rangle_j \langle r|, \end{aligned} \quad (\text{A10})$$

where $D_j \approx 2.88$ GHz is the zero-field splitting (ZFS) of the j th center and $E_j < 10$ MHz, and $g_e = 2.0028$, $\mu_B = 14$ MHz mT^{-1} . Each NV^- center has slightly different zero-field splitting D_j due to the slightly different local strain in the crystal. We define the statistic average ZFS as $\bar{D} = \sum_j P_j D_j$ with P_j the probability of D_j and the derivation $\delta_j = D_j - \bar{D}$. Generally, the flux qubit can generate a magnetic field \mathbf{B}_q along the direction of S_z or $S_{x,y}$. In our setup, we assume that the \mathbf{B}_q orients along the S_x direction. $S_{x,y,z}$ represent the spin 1 operators of the NV^- centers and have the forms

$$S_z = \begin{matrix} & |m_s = +1\rangle & |m_s = 0\rangle & |m_s = -1\rangle \\ \begin{matrix} |m_s = +1\rangle \\ |m_s = 0\rangle \\ |m_s = -1\rangle \end{matrix} & \begin{pmatrix} 1 & 0 & 0 \\ 0 & 0 & 0 \\ 0 & 0 & -1 \end{pmatrix} \end{matrix},$$

$$S_x = \frac{1}{\sqrt{2}} \begin{matrix} & |m_s = +1\rangle & |m_s = 0\rangle & |m_s = -1\rangle \\ \begin{matrix} |m_s = +1\rangle \\ |m_s = 0\rangle \\ |m_s = -1\rangle \end{matrix} & \begin{pmatrix} 0 & 1 & 0 \\ 1 & 0 & 1 \\ 0 & 1 & 0 \end{pmatrix} \end{matrix},$$

$$S_y = \frac{1}{\sqrt{2}} \begin{matrix} & |m_s = +1\rangle & |m_s = 0\rangle & |m_s = -1\rangle \\ \begin{matrix} |m_s = +1\rangle \\ |m_s = 0\rangle \\ |m_s = -1\rangle \end{matrix} & \begin{pmatrix} 0 & -i & 0 \\ i & 0 & -i \\ 0 & i & 0 \end{pmatrix} \end{matrix},$$

$$S_z^2 = \begin{matrix} & |m_s = +1\rangle & |m_s = 0\rangle & |m_s = -1\rangle \\ \begin{matrix} |m_s = +1\rangle \\ |m_s = 0\rangle \\ |m_s = -1\rangle \end{matrix} & \begin{pmatrix} 1 & 0 & 0 \\ 0 & 0 & 0 \\ 0 & 0 & 1 \end{pmatrix} \end{matrix},$$

$$S_x^2 - S_y^2 = \begin{matrix} & |m_s = +1\rangle & |m_s = 0\rangle & |m_s = -1\rangle \\ \begin{matrix} |m_s = +1\rangle \\ |m_s = 0\rangle \\ |m_s = -1\rangle \end{matrix} & \begin{pmatrix} 0 & 0 & -1 \\ 0 & 0 & 0 \\ -1 & 0 & 0 \end{pmatrix} \end{matrix}.$$

We define $|+\rangle = (|^3\text{A}_2, m_s = +1\rangle + |^3\text{A}_2, m_s = -1\rangle)/\sqrt{2}$ and $|-\rangle = (|^3\text{A}_2, m_s = +1\rangle - |^3\text{A}_2, m_s = -1\rangle)/\sqrt{2}$ so that $S_x^2 - S_y^2 = -(|^3\text{A}_2, m_s = +1\rangle \langle ^3\text{A}_2, m_s = -1| + |^3\text{A}_2, m_s = -1\rangle \langle ^3\text{A}_2, m_s = +1|) = (|-\rangle \langle -| - |+\rangle \langle +|)$. The term $E_j(S_{x,j}^2 - S_{y,j}^2)$ only shifts the state $|+\rangle = (|^3\text{A}_2, m_s = +1\rangle + |^3\text{A}_2, m_s = -1\rangle)/\sqrt{2}$ down by energy E_j . It can be absorbed in D_j when we study the coupling between $|^3\text{A}_2, m_s = 0\rangle \leftrightarrow |+\rangle$. The term $B_{z,j} S_{z,j}$ describes the Zeeman splitting due to the magnetic field applied to the z direction.

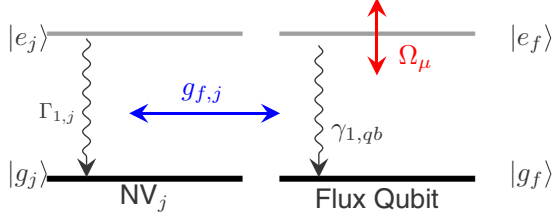


FIG. 7. (Color online) Diagram of the interaction between the flux qubit and the j th NV^- center. The states are defined as $|g_j\rangle = |^3\text{A}_2, m_s = 0\rangle_j$ and $|e_j\rangle = (|^3\text{A}_2, m_s = +1\rangle_j + |^3\text{A}_2, m_s = -1\rangle_j)/\sqrt{2}$. The NV center and the flux qubit decay with rates $\Gamma_{1,j}$ and $\gamma_{1,qb}$, respectively. The flux qubit couples to the magnetic transition of the two ground states $|e_j\rangle$ and $|g_j\rangle$ of the j th NV center with the rate $g_{f,j}$. The transition frequency of the qubit is sine modulated with the amplitude of Ω_μ and the frequency ω_μ .

A reasonable large magnetic field also can be used to lift the degeneracy between $|m_s = \pm 1\rangle$ levels, and subsequently excludes the transition of $|m_s = 0\rangle \leftrightarrow |m_s = -1\rangle$ [12]. This term is assumed to be negligible ($B_{z,j} \approx 0$) through our investigation following.

The flux qubit couples to the ensemble of NV^- centers via the magnetic field created by its persistent current. To study the magnetic interaction between these two quantum subsystems, we only consider the triplet ground state of the NV's electric spin in this stage. In order to match the experimental setup [8], we consider the transition of $|g_j\rangle \leftrightarrow |e_j\rangle$, as shown in Fig. 7.

We assume that the magnetic field $\mathbf{B}_{q,j}$ created by the flux qubit orients to the x direction of the j th center so that it is parallel to S_x . Thus, we have $\mathbf{B}_{q,j} = B_{x,j} = \frac{\mu_0 I_p}{2\mathcal{R}_j} \sigma'_z$ [8], where $\mathcal{R}_j = \sqrt{\mathcal{D}^2 + d_j^2}$ with \mathcal{D} the distance from the flux qubit to the center of the flux loop and d_j the distance from the center of the flux loop to the ensemble center. Generally, R_j denotes the distance between the flux qubit and the j th NV^- center. Then, the interaction Hamiltonian describing the coupling between the flux qubit and the NV^- centers is

$$H_{Q-\text{NV}} = \sum_j g_{f,j} S_{x,j} \sigma'_z = \sum_j g_{f,j} S_{x,j} \sigma_x, \quad (\text{A11})$$

where $g_{f,j}/2\pi = \frac{g_e \mu_0 \mu_B I_p}{\mathcal{R}_j} \sim 4.4$ kHz in [8] for $\mathcal{D} = 0.7$ μm and $d_j = 1$ μm . μ_0 is the vacuum permeability (we have used $\sigma'_z = \cos\theta\sigma_z + \sin\theta\sigma_x \Rightarrow \sigma'_z = \sigma_x$ when $\mathcal{T} \gg \epsilon$ yielding $\sin\theta \approx 1$). We now assume that the wavelength corresponding to the microwave transition of the flux qubit to be much larger than the size of diamond crystal and from this we can neglect the phase diffusion in the coupling $g_{f,j}$.

The Hamiltonian for our flux qubit coupled to an ensemble of NV^- centers can be represented by

$$H = \frac{\omega_q}{2} \sigma_z + \sum_j D_j S_{z,j}^2 + \sum_j g_{f,j} S_{x,j} \sigma_x. \quad (\text{A12})$$

c. Modeling the interaction between flux qubits and a rare-earth ion doped crystal $\text{Er}^{3+} : \text{Y}_2\text{SiO}_5$

An ensemble of rare-earth Er^{3+} ion doped in Y_2SiO_5 crystal is another promising candidate for the quantum interface transferring quantum information from optical to microwave

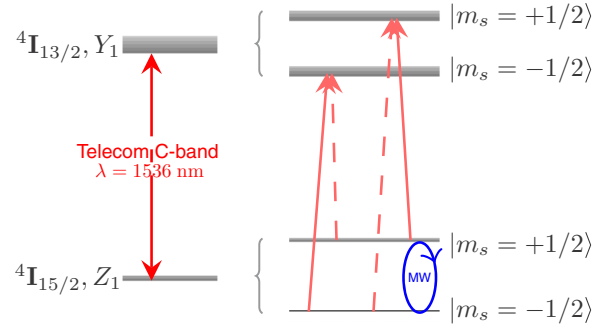


FIG. 8. (Color online) Level diagram of a rare-earth ion Er^{3+} in crystal Y_2SiO_5 allowing an optical Raman transition and a microwave transition [7,18,35].

and vice versa. It has significant advantages: (i) The two electronic ground states have a large- g factor up to 15. (ii) The concentration of ions in the hosting crystal can be very large. These two unique properties allow it to strongly couple to a flux qubit. (iii) It has long-lived optical and microwave lifetimes. (iv) It works in both optical telecom C-band around 1.55 μm and microwave C-band round 4–9 GHz. We next discuss here how our scheme can be extended to the rare-earth ion crystal.

As shown in Fig. 8, both the excited state $^4\text{I}_{13/2} : Y_1$ and the ground states $^4\text{I}_{15/2} : Z_1$ for each Er^{3+} ion are doublets. The optical transition $^4\text{I}_{15/2} : Z_1 \rightarrow ^4\text{I}_{13/2} : Y_1$ and the microwave transition $|^4\text{I}_{15/2} : Z_1, m_s = -1/2\rangle \rightarrow |^4\text{I}_{15/2} : Z_1, m_s = +1/2\rangle$ form two Λ -type systems [7,18,35]. In the dispersive coupling regime, we can model the system as a simple Λ -type system with one excited state $|r_j\rangle = |^4\text{I}_{13/2} : Y_1\rangle$, two ground states $|e_j\rangle = |^4\text{I}_{15/2} : Z_1, m_s = +1/2\rangle$ and $|g_j\rangle = |^4\text{I}_{15/2} : Z_1, m_s = -1/2\rangle$. The electric dipole moment of the optical transition is about 2.07×10^{-32} C m, while the g factor for the magnetic coupling depends on the orientation of the extinction axis and can be up to 15 [25,35], yielding a spin tuning rate (Zeeman splitting) up to 200 GHz/T [7]. The optical transition is at around $\lambda \sim 1536$ nm, while the zero-field splitting of the two ground states is around 4 GHz [36].

The Hamiltonian of an ensemble of rare-earth ions including the magnetic coupling is given by [7,25]

$$H_{\text{Er}} = \sum_j \frac{D_j}{2} \tilde{S}_{z,j} + \mu_B \mathbf{B}_j \cdot \mathbf{g}_e \cdot \tilde{\mathbf{S}}_j + \omega_{r,j} |r_j\rangle \langle r_j|, \quad (\text{A13})$$

where D_j is the zero-field splitting of the j th spin, \mathbf{B}_j denotes the external magnetic field applied to the j th spin and are slightly different because it is inhomogeneous at different sites of the spins. \mathbf{g}_e is the g -factor tensor, and the electronic spin operator $\tilde{\mathbf{S}}_j$ are defined as $\{\tilde{S}_{z,j}, \tilde{S}_{x,j}, \tilde{S}_{y,j}\} = \{|^4\text{I}_{15/2} : Z_1, m_s = +1/2\rangle \langle ^4\text{I}_{15/2} : Z_1, m_s = +1/2| - |^4\text{I}_{15/2} : Z_1, m_s = -1/2\rangle \langle ^4\text{I}_{15/2} : Z_1, m_s = -1/2|, |^4\text{I}_{15/2} : Z_1, m_s = +1/2\rangle \langle ^4\text{I}_{15/2} : Z_1, m_s = -1/2| + |^4\text{I}_{15/2} : Z_1, m_s = -1/2\rangle \langle ^4\text{I}_{15/2} : Z_1, m_s = +1/2|, -i(|^4\text{I}_{15/2} : Z_1, m_s = +1/2\rangle \langle ^4\text{I}_{15/2} : Z_1, m_s = -1/2| - |^4\text{I}_{15/2} : Z_1, m_s = -1/2\rangle \langle ^4\text{I}_{15/2} : Z_1, m_s = +1/2|)\}$. Here, we neglect the hyperfine interaction and the nuclear quadrupole

interaction and $\omega_{r,j}$ is the energy of the optical excited state $|r_j\rangle$.

We use the arrangement similar to the qubit-NV system discussed above [8] such that the magnetic field created by the flux qubit orients to the local x direction of the ions. When the rare-earth ions are inserted within the loop of the flux qubit, the magnetic coupling between these two systems is described by [25]

$$H_{Q\text{-Er}} = \sum_j^N g_{f,j} \tilde{S}_{x,j} \sigma_x. \quad (\text{A14})$$

As a result, the Hamiltonian describing the evolution of the spins and the flux qubit is given by

$$H = \frac{\omega_q}{2} \sigma_z + \sum_j^N \frac{D_j}{2} \tilde{S}_{z,j} + g_{f,j} \tilde{S}_{x,j} \sigma_x. \quad (\text{A15})$$

Because there is only one excitation in the system at most, we can consider the motion of the system in the one-excitation basis. We instead use the notations $\tilde{S}_{z,j} = |e_j\rangle\langle e_j| - |g_j\rangle\langle g_j|$, $\tilde{S}_{+,j} = |e_j\rangle\langle g_j|$, $\tilde{S}_{-,j} = |g_j\rangle\langle e_j|$. After applying the unitary transform $U = e^{-i(\frac{\tilde{D}}{2}\sigma_z + \sum_j^N \tilde{D} \tilde{S}_{z,j}^2)t}$ to Eq. (A12) or $U = e^{-i(\frac{\tilde{D}}{2}\sigma_z + \sum_j^N \frac{\tilde{D}}{2} \tilde{S}_{z,j})t}$ to Eq. (A15), and the rotating-wave approximation, we have the Hamiltonian describing the general qubit-spin system

$$H_{Q\text{-spin}} = \frac{\Delta_q}{2} \sigma_z + \sum_j^N \frac{\delta_j}{2} \tilde{S}_{z,j} + g_{f,j} (\tilde{S}_{+,j} \sigma_- + \sigma_+ \tilde{S}_{-,j}) \quad (\text{A16})$$

with $\Delta_q = \omega_q - \bar{D}$. Under cryogenic temperature, we may assume that the spins remain in $|g_j\rangle$ if they are initialized in that state because D_j is a few GHz ($D_j \approx 2\pi \times 2.88$ GHz [8] for NV⁻ centers and $D_j \approx 2\pi \times 4$ GHz [36] for Er ions).

d. Interaction in the single-excitation space

We model the case in which a single excitation is injected into the system via the flux qubit. It allows one to consider the one-excitation space (OES) whose spanning state vectors are each $N + 2$ long and can be written as

$$\begin{aligned} |g_f, G\rangle &= |g_f, g_1, g_2, \dots, g_M\rangle = |0\rangle_M, \\ |e_f, G\rangle &= |e_f, g_1, g_2, \dots, g_M\rangle = |1\rangle_M, \\ |g_f, \dot{e}_j\rangle &= |g_f, g_1, g_2, \dots, g_{j-1}, e_j, g_{j+1}, \dots, g_M\rangle = |j+1\rangle_M, \end{aligned} \quad (\text{A17})$$

$j \in \{1, 2, \dots, N\}$. We thus have $M = N + 2$ eigenstates in the OES.

Setting the state $|g_f, G\rangle$ as the zero-energy level in the OES, one can find the following OES representations:

$$\sigma_z = \begin{pmatrix} -1 & 0 & 0 & \dots & 0 \\ 0 & 1 & 0 & \dots & 0 \\ 0 & 0 & 0 & \dots & 0 \\ \vdots & \vdots & \vdots & \ddots & \vdots \\ 0 & 0 & 0 & \dots & 0 \end{pmatrix} = |1\rangle_M\langle 1| - |0\rangle_M\langle 0|,$$

$$\sigma_- = \begin{pmatrix} 0 & 1 & 0 & \dots & 0 \\ 0 & 0 & 0 & \dots & 0 \\ \vdots & \vdots & \vdots & \ddots & \vdots \\ 0 & 0 & 0 & \dots & 0 \end{pmatrix} = |0\rangle_M\langle 1|,$$

$$\tilde{S}_{z,j} = |j+1\rangle_M\langle j+1| - |0\rangle_M\langle 0|,$$

and

$$\tilde{S}_{-,j} = |0\rangle_M\langle j+1|.$$

Using the notations $\{|l\rangle_M\}$ for the OES, the operators take the forms

$$\begin{aligned} \sigma_z &= |1\rangle_M\langle 1| - |0\rangle_M\langle 0|, \\ \sigma_- &= |0\rangle_M\langle 1|, \\ \tilde{S}_{z,j} &= |j+1\rangle_M\langle j+1| - |0\rangle_M\langle 0|, \\ \tilde{S}_{-,j} &= |0\rangle_M\langle j+1|. \end{aligned} \quad (\text{A18})$$

By defining the operator

$$\begin{aligned} \mathbb{I} &= \sum_{l=0}^{N+1} |l\rangle_M\langle l| \\ &= |g_f, G\rangle\langle g_f, G| + |e_f, G\rangle\langle e_f, G| + \sum_{j=1}^N |g_f, \dot{e}_j\rangle\langle g_f, \dot{e}_j|, \end{aligned}$$

we also find

$$\begin{aligned} \sigma_z &= |1\rangle_M\langle 1| - \sum_j |j+1\rangle_M\langle j+1| - |0\rangle_M\langle 0| \\ &= 2|1\rangle_M\langle 1| - \mathbb{I} \end{aligned} \quad (\text{A19})$$

and

$$\begin{aligned} \tilde{S}_{z,j} &= |j+1\rangle_M\langle j+1| \\ &\quad - \sum_{l \neq j} |l+1\rangle_M\langle l+1| - |0\rangle_M\langle 0| - |1\rangle_M\langle 1| \\ &= 2|j+1\rangle_M\langle j+1| - \mathbb{I}. \end{aligned}$$

Since we can drop \mathbb{I} in the Hamiltonian, we can then have

$$\sigma_z = 2\sigma_+\sigma_-, \quad (\text{A20})$$

$$\tilde{S}_{z,j} = 2\tilde{S}_{+,j}\tilde{S}_{-,j}, \quad (\text{A21})$$

where all operators are represented in the OES. Thus, the Hamiltonian describing the full system of coupled flux-qubit-spin ensemble takes the form

$$\begin{aligned} H_{Q\text{-spin}} &= \Delta_q \sigma_+ \sigma_- + \sum_j \delta_j \tilde{S}_{+,j} \tilde{S}_{-,j} \\ &\quad + g_{f,j} (\tilde{S}_{+,j} \sigma_- + \sigma_+ \tilde{S}_{-,j}), \end{aligned} \quad (\text{A22})$$

or in matrix form by

$$H_{Q\text{-spin}} = \begin{pmatrix} |g_f, G\rangle \\ |e_f, G\rangle \\ |g_f, \dot{e}_1\rangle \\ \vdots \\ |g_f, \dot{e}_{j-1}\rangle \\ |g_f, \dot{e}_j\rangle \\ |g_f, \dot{e}_{j+1}\rangle \\ \vdots \\ |g_f, \dot{e}_N\rangle \end{pmatrix} \begin{pmatrix} |g_f, G\rangle & |e_f, G\rangle & |g_f, \dot{e}_1\rangle & \dots & |g_f, \dot{e}_{j-1}\rangle & |g_f, \dot{e}_j\rangle & |g_f, \dot{e}_{j+1}\rangle & \dots & |g_f, \dot{e}_N\rangle \\ 0 & 0 & 0 & \dots & 0 & 0 & 0 & \dots & 0 \\ 0 & \Delta_q & g_{f,1} & \dots & g_{f,j-1} & g_{f,j} & g_{f,j+1} & \dots & g_{f,N} \\ 0 & g_{f,1} & \delta_1 & \dots & 0 & 0 & 0 & \dots & 0 \\ \vdots & \vdots & \vdots & \ddots & \vdots & \vdots & \vdots & \ddots & \vdots \\ 0 & g_{f,j-1} & 0 & \dots & \delta_{j-1} & 0 & 0 & \dots & 0 \\ 0 & g_{f,j} & 0 & \dots & 0 & \delta_j & 0 & \dots & 0 \\ 0 & g_{f,j+1} & 0 & \dots & 0 & 0 & \delta_{j+1} & \dots & 0 \\ \vdots & \vdots & \vdots & \ddots & \vdots & \vdots & \vdots & \ddots & \vdots \\ 0 & g_{f,N} & 0 & \dots & 0 & 0 & 0 & \dots & \delta_N \end{pmatrix}.$$

The decoherence superoperators for dissipation and pure dephasing for each NV⁻ center are given by

$$\mathcal{L}_{\text{spin},j}^{(1)}\rho = \frac{\Gamma_{1,j}}{2}\{2\bar{S}_{-,j}\rho\bar{S}_{+,j} - \bar{S}_{+,j}\bar{S}_{-,j}\rho - \rho\bar{S}_{+,j}\bar{S}_{-,j}\}, \quad (\text{A23})$$

$$\mathcal{L}_{\text{spin},j}^{(2)}\rho = \Gamma_{2,j}^*(\bar{S}_{z,j}\rho\bar{S}_{z,j} - \rho), \quad (\text{A24})$$

where $\Gamma_{1,j}$ and $\Gamma_{2,j}^*$ are the depopulation and pure dephasing rates of the state $|e_j\rangle$ in the j th NV⁻ center or spin. Combining all this, we can simulate the dynamics of the full system using the Lindblad master equation

$$\begin{aligned} \frac{\partial \rho}{\partial t} = & -i[H_{Q\text{-spin}}, \rho] + \mathcal{L}_q^{(1)}[\rho] + \mathcal{L}_q^{(2)}[\rho] \\ & + \sum_j \mathcal{L}_{\text{spin},j}^{(1)}[\rho] + \sum_j \mathcal{L}_{\text{spin},j}^{(2)}[\rho], \end{aligned} \quad (\text{A25})$$

where the Hamiltonian takes the form given by Eq. (A22).

e. Confirmation of the model with experimental data

To study the performance of the quantum interface between optical and microwave, our single-excitation model describing the interaction of the ensemble of spins and the flux qubit considers the inhomogeneous broadening of the transition frequencies of the spins. This is an *important difference* between our model and that used in [8]. Before discussing the quantum interface, we first justify the validity of our model by a near perfect matching with the experimental data presented in [8]. The parameters given by Zhu *et al.* are described in Tables I and II and their values are listed in Tables III, IV, V, and VI.

Although Zhu *et al.* reproduced well the experimental result of the vacuum Rabi oscillation curve by varying the T_1 and T_2 of the flux qubit and the NV centers, we instead first explore the validity of assuming homogeneous decay and dephasing rates for the diamond subsystem. With this assumption we achieve a poor agreement with the experiment for the Rabi oscillation over the whole duration with only good agreement during the first period of oscillation. Our best fit is shown in Fig. 9 using the homogeneous parameters listed in Tables VII and VIII. Obviously, we successfully reproduce the first Rabi oscillation, however, we note that more population than predicted by the

model returns to the flux qubit during the period from ~ 20 to ~ 60 ns.

We understand this excess qubit population to be mainly due to a dark-state-related strengthening of the revival of the qubit population due to an inhomogeneous broadening in the transition frequencies of the spins. When the inhomogeneous broadening of the transition frequencies of the spin ensemble is small in comparison with the ensemble-qubit coupling rate, this inhomogeneity creates a slow decay channel from the single-excitation state (or bright state), to a multitude of spin dark states which are relatively long lived. This inhomogeneous broadening can be considered as an additional decay of the single-excitation bright state of the spins [12,37–39] during the first few Rabi oscillation periods. However, if the inhomogeneous broadening is comparable to the coupling rate, one can have cycling from the multitude of dark state bath to the bright state. To consider this effect, we expand our model to encompass a distribution (inhomogeneity) of transition frequencies for the spin ensemble. It can be clearly seen from Fig. 10 that this model correctly reproduces the emergence of the large population of the flux qubit when $t > 20$ ns. The parameters listed in Tables IX–XI are used in this extended inhomogeneous model. We will use this model including the broadening of the transition frequencies of the spin ensemble for our numerical investigations throughout the remainder of our study below and in the main manuscript.

The parameters of the flux qubit and the NV centers for our fit in Fig. 10 are listed in Tables IX and X. Obviously, the decay rate of the flux qubit is small. Interestingly, although

TABLE I. Description of parameters of the flux qubit.

Notation	Description
I_p	Persistent current
$\gamma_{1,qb}$	Relaxation rate
$T_{1,qb}$	Relaxation time
$\gamma_{2,qb}^*$	Pure dephasing rate
$T_{2,qb}$	Dephasing time
$T_{2,qb}^*$	Pure dephasing time
Δ	Representing the detuning between the flux qubit and the magnetic transition of the spins (NV centers)
B	Magnetic field created the flux qubit
σ_Δ	Inhomogeneity of the detuning Δ

TABLE II. Description of parameters of the spins (NV centers).

Notation	Description
D	Zero-field splitting of the ground states
g_e	g factor of the electron
E	Strain-induced splitting
γ_{en}	Relaxation rate of the ensemble of spins
Γ_2^*	Pure dephasing rate of the ensemble of spins
$T_{1,en}^*$	Relaxation time of the ensemble of spins
$T_{2,en}$	Dephasing time of the ensemble of spins
$T_{2,en}^*$	Pure dephasing time of the ensemble of spins
\mathcal{R}	Distance from the flux qubit to the center of the ensemble of spins
$B_{NV,z}$	Magnetic field along S_z of the ensemble of the spins. It is applied to tune the Zeeman splitting.
N	Total number of spins (NV centers) in the ensemble
N_g	Group numbers of the spins (NV centers). It means that we divided all spins into N_g groups, in which the spins are considered as identical, for simulations
g_f	Magnetic coupling rate of the flux qubit to one group of spins
\bar{g}_i	Collective coupling rate of the total spins to the flux qubit
σ_δ	Inhomogeneous broadening of the zero-field splitting D_j of the spins. It means that the parameter D_j varies within a variance of σ_δ as a random number in simulations
$\sigma_{\Gamma_{1,j}}$	Inhomogeneous broadening of the relaxation rate of the spins. It means that the parameter $\Gamma_{1,j}$ varies within a variance of $\sigma_{\Gamma_{1,j}}$ as a random number in simulations
$\sigma_{\Gamma_{2,j}^*}$	Inhomogeneous broadening of the pure dephasing rate of the spins. It means that the parameter $\Gamma_{1,j}$ varies within a variance of $\sigma_{\Gamma_{2,j}^*}$ as a random number in simulations
σ_{g_f}	Inhomogeneity in the grouped coupling rate g_f . It represents that the parameter g_f varies within a variance of σ_{g_f} as a random number in simulations

TABLE III. Parameters of the flux qubit in [8].

I_p (mA)	$\gamma_{1,qb}/2\pi$ (MHz)	$\Delta/2\pi$ (nHz)	$\gamma_{2,qb}^*/2\pi$ (MHz)
300	1	0	

TABLE IV. Parameters of the NV^- centers in [8].

$D/2\pi$ (GHz)	g_e	μ_B (MHz mT $^{-1}$)	$E/2\pi$ (MHz)	$\gamma_{en}/2\pi$ (MHz) (on resonance)	$\Gamma_2^*/2\pi$	B B	\mathcal{R} (μ m)	Density cm $^{-3}$	N	$g_i/2\pi$ (kHz)	$\bar{g}_i/2\pi = \sqrt{N}g_i/2\pi$ (MHz)
2.88	2.0028	14	0(< 10)	~ 8 (~ 20 ns)		$\frac{\mu_0 I_p}{2\mathcal{R}}$	1.2	5×10^{18}	3×10^7	4.4	35

TABLE V. Parameters of the flux qubit in [12].

I_p (mA)	$T_{1,qb}$ (ns)	$T_{2,qb}$ (ns) away from sweet point	$T_{2,qb}$ (ns) at sweet point	$T_{2,qb}^* = [T_{2,qb}^{-1} - (2T_{1,qb})^{-1}]^{-1}$ (ns)
	395	19.7	100	20.2 (for $T_{2,qb} = 19.7$ ns); 114 (for $T_{2,qb} = 100$ ns)

TABLE VI. Parameters of the NV^- centers in [12].

$D/2\pi$ (GHz)	$B_{NV,z}$ (mT)	$E/2\pi$ (MHz)	$T_{1,en}^*$ (ns)	$T_{2,en}^*$ (ns) (pure dephasing)	$T_{2,en} = [(2T_{1,en})^{*-1} + T_{2,en}^{*-1}]^{-1}$ (ns)	B B	$(D_+ - D_-)/2\pi$ (MHz)	Density cm $^{-3}$	N	$g_i/2\pi$ (kHz)	$\bar{g}_i/2\pi = \sqrt{N}g_i/2\pi$ (MHz)
2.878	2.67	4	20.8	175	33.6	$\frac{\mu_0 I_p}{2\mathcal{R}}$	~ 40	4.7×10^{17}	10^7	4.4	8.9

TABLE VII. Parameters of the flux qubit for our fit in Fig. 9.

$\gamma_{1,qb}/2\pi$ (MHz)	$\gamma_{2,qb}^*/2\pi$ (MHz)	$\sigma_\Delta/2\pi$ (MHz)	$\Delta/2\pi$ (MHz) detuning
0.4	1	0	0

we set the detuning $\Delta = 0$ in our simulations, the random broadening in D_j gives an effective detuning of $2\pi \times 5.8$ MHz which we believe comes from the energy shift due to the strain-induced splitting E . To do the simulations, we divided the NV centers into 20 groups. There is no observable change when we increase the number of groups to 40.

In Fig. 10, we consider an inhomogeneous model where some parameters vary throughout the ensemble of NV centers. The extent of these variations is characterized in Table XI. The parameter variances used in Table XI are defined as $\sigma_X = \sqrt{\sum_j^N (\bar{X} - X_j)^2 / N}$ with $X_j \in \{\Delta_j, \Gamma_{1,j}, \Gamma_{2,j}, g_{f,j}\}$, where $\bar{X} = \langle X_j \rangle$ is the statistic average value. Note that the decay rate $\Gamma_{1,en}^*/2\pi = 28$ MHz of the NV⁻ centers in the first model is somewhat close to the sum of the collective decay rate of $\Gamma_{1,en}^*$ and the inhomogeneous broadening in the transition frequency σ_δ in the second model. It provides strong evidence that the inhomogeneous broadening plays a role of the decay in short time [37–39].

2. Transfer quantum information between qubit and cavity via sideband transition

In this section, we show how to use the technique of stimulated Raman adiabatic passage (STIRAP) to transfer quantum information between the flux qubit and the cavity mode robust against the inhomogeneity and decoherence of the ensemble of spins.

In the widely studied schemes by Zhu *et al.* [8], etc., the coupling of the flux qubit to the ensemble of spins is constant in time. As a result, to switch off the interaction with the spins, the flux qubit must be biased far away from the “sweet spot” which causes a large decoherence. We next present a method to modulate the qubit coupling via the sideband transition. One of the advantages of this sideband-transition scheme is that one can efficiently tune on and off the flux-qubit–spin interaction while the qubit remains at the “sweet spot” where the decoherence is lowest. More importantly, the sideband-transition scheme enables the STIRAP technique and avoids much excitation of the ensemble of spins, and subsequently greatly suppresses the unwanted influence of the inhomogeneity of the spins on the quantum transfer.

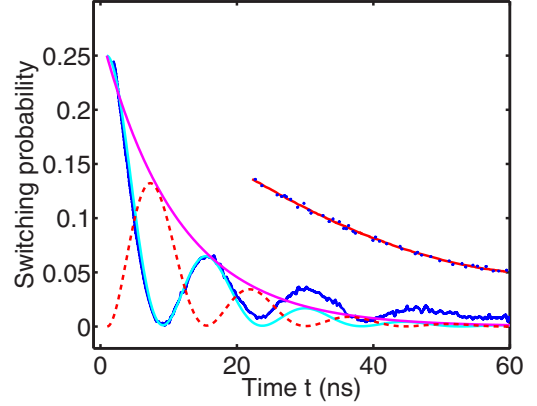


FIG. 9. (Color online) Predicting the experimental data of the Rabi oscillation in [8] assuming homogeneity in the NV ensemble. Blue line and dots are the experimental measurement data taken from [8]. Magenta line shows the decay rate we use for fitting. Cyan line for the switching probability as a fitting of the Rabi oscillation. The pure damping data (blue dots) are fitted using $e^{-2\pi t/150}$ (corresponding to a decay rate of $2\pi \times 1$ MHz).

a. Modulation of the qubit-spin-cavity interaction

Here, we consider a hybrid quantum system consisting of a flux qubit, an ensemble of spins, and an optical cavity shown in Fig. 11. The scheme depicting the coupling between the flux qubit and the spin ensemble for one node is shown in Fig. 12. In the level diagram of the spins, $|r_j\rangle = |^3E, S_z\rangle$ for NV centers, while $|r_j\rangle = |^4I_{13/2} : Y_1\rangle$ for Er³⁺ ions. As before, we neglect the terms $\sum_j^N g_e \mu_e B_{z,j} S_{z,j} + E_j (S_{x,j}^2 - S_{y,j}^2)$ in the NV centers. For NV centers, $B_{z,j}$ can be large enough to split $|m_s = +1\rangle$ and $|m_s = -1\rangle$ such that the splitting is much larger than E_j . When a σ_+ -polarized control field Ω_c is applied, the fields and qubit only couple to the transitions $|r_j\rangle \leftrightarrow |m_s = +1_j\rangle$ and $|m_s = 0_j\rangle \leftrightarrow |m_s = +1_j\rangle$, respectively. Alternatively, we also can arrange that $B_j \sim 0$ and the control field Ω_c is linearly polarized. Thus, Ω_c optically and the qubit magnetically couple to the transitions $|r_j\rangle \leftrightarrow (|m_s = +1_j\rangle + |m_s = -1_j\rangle)/\sqrt{2}$ and $|g_j\rangle \leftrightarrow (|m_s = +1_j\rangle + |m_s = -1_j\rangle)/\sqrt{2}$, respectively. Either way, we can replace the states $|m_s = +1_j\rangle$ or $(|m_s = +1_j\rangle + |m_s = -1_j\rangle)/\sqrt{2}$ with $|e_j\rangle$. For rare-earth ions, we simply have $|e_j\rangle = |^4I_{15/2} : Z_1, m_s = +1/2\rangle$ and $|g_j\rangle = |^4I_{15/2} : Z_1, m_s = -1/2\rangle$. The Hamiltonian related to the free evolution of the NV centers or the rare-earth ions takes the form

$$H_{NV} = \sum_j^N D_j S_{z,j}^2 + \omega_{r,j} |r_j\rangle \langle r_j|, \quad (\text{A26a})$$

TABLE VIII. Parameters of the NV centers for our fit in Fig. 9.

$D/2\pi$ (GHz)	$B_{NV,z}$ (mT)	$E/2\pi$ (MHz)	$\Gamma_{1,en}^*/2\pi$ (MHz)	$\Gamma_{2,en}^*/2\pi$ (pure dephasing)	$T_{2en}^{-1} = 2T_{1en}^{*-1} + T_{2en}^{*-1}$ (ns)	N_g groups	$(D_+ - D_-)/2\pi$ (MHz)	Density cm^{-3}	N	$g_f/2\pi$ (MHz) grouped coupling	$\bar{g}_i/2\pi = \sqrt{N} g_i/2\pi$ (MHz)
2.878	0	<10	28	0.9	33.6	40	~0	5×10^{18}	1.6×10^7	5.56	35

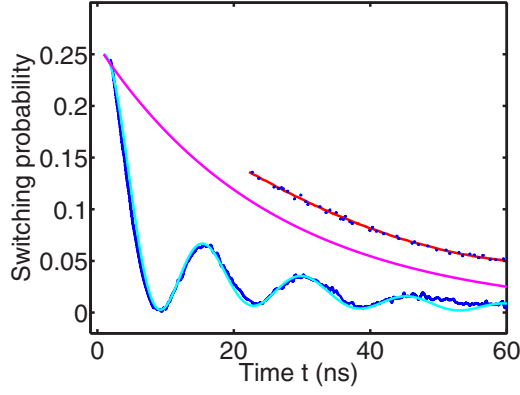


FIG. 10. (Color online) As in Fig. 9 but including inhomogeneity in the transition frequencies of the spin ensemble, the coupling rates $g_{f,j}$, and the decoherence rates.

$$H_{\text{Er}} = \sum_j^N \frac{D_j}{2} S_{z,j} + \omega_{r,j} |r_j\rangle \langle r_j|. \quad (\text{A26b})$$

We set the energy of the ground state $|g_j\rangle$ to be zero. Using this, the free Hamiltonians (A26) and the optical-spin interaction can be rewritten both as

$$H_{\text{spin0}} = \sum_j D_j |e_j\rangle \langle e_j| + \omega_{r,j} |r_j\rangle \langle r_j|, \quad (\text{A27})$$

$$H_{o\text{-spin}} = \sum_j (g_{c,j} e^{ikR_j} \hat{a}_j^\dagger |g_j\rangle \langle r_j| + g_{c,j} e^{-ikR_j} \hat{a} |r_j\rangle \langle g_j|) + \sum_j \Omega_c (e^{i\omega_L t + i\phi(t)} |e_j\rangle \langle r_j| + e^{-i\omega_L t - i\phi(t)} |r_j\rangle \langle e_j|). \quad (\text{A28})$$

This system including three subsystems {flux qubit, spin ensemble, cavity mode} can be described by the Hamiltonian H_{node} in Eq. (A29):

$$H_{\text{node}} = H_q + H_{\text{spin0}} + H_c + H_{q\text{-spin}} + H_{o\text{-spin}}, \quad (\text{A29})$$

$$H_q = \frac{\omega_q}{2} \sigma_z + \Omega_\mu \cos(\omega_\mu t) \sigma_z, \quad (\text{A30})$$

$$H_c = \omega_c \hat{a}^\dagger \hat{a}, \quad (\text{A31})$$

$$H_{q\text{-NV}} = \sum_j^N g_{f,j} \sigma_x S_{x,j}, \quad (\text{A32})$$

where R_j is the position of the j th NV center. The JC coupling between the cavity mode \hat{a} and the j th NV center is given through the coupling strength $g_{c,j}$ and the phase ikR_j which

is inhomogeneous because this optical phase is sensitive to the site of the spins R_j . The Raman control field has a frequency ω_L , and Rabi frequency Ω_c , and a nontrivial phase $\phi(t)$.

We next apply the unitary transform

$$\begin{aligned} \hat{U} = & \exp\{-i[(\omega_{r,j} - \omega_L)t - \phi]|e_j\rangle \langle e_j|\} \\ & \otimes \exp\{-i\omega_r t |r_j\rangle \langle r_j| - i(\omega_{r,j} - \omega_c)t |g_j\rangle \langle g_j|\} \\ & \otimes \exp\left\{-i\omega_c t \hat{a}^\dagger \hat{a} - i\left[\frac{\omega_q}{2} t \sigma_z + \frac{\Omega_\mu}{\omega_\mu} \sin(\omega_\mu t) \sigma_z - \frac{\phi}{2} \sigma_z\right]\right\} \end{aligned}$$

to the full system and define $\Delta_j = \omega_{r,j} - \omega_r$ with $\omega_r = \langle \omega_{r,j} \rangle$, $\delta = \omega_L - \omega_c$, $\Delta_0 = \omega_r - \omega_c$, and $\Delta_1 = (\omega_r - \omega_L) - \bar{D}$, $\Delta_q = \omega_q - \delta$. From this we have the relations

$$\Delta_1 - \Delta_0 = \delta - \bar{D}. \quad (\text{A33})$$

Under the two-photon resonance condition, $\delta = \bar{D}$. From this, we have [40–43]

$$\begin{aligned} \hat{H} = & \frac{\dot{\phi}}{2} \sigma_z - \sum_j (\Delta_1 + \Delta_j - \delta_j - \dot{\phi}) |e_j\rangle \langle e_j| \\ & - \sum_j (\Delta_0 + \Delta_j) |g_j\rangle \langle g_j| \\ & + \sum_j \Omega_c (|e_j\rangle \langle r_j| + |r_j\rangle \langle e_j|) \\ & + \sum_j (g_{c,j} e^{ikR_j} \hat{a}_j^\dagger |g_j\rangle \langle r_j| + g_{c,j} e^{-ikR_j} \hat{a} |r_j\rangle \langle g_j|) \\ & + \sum_j g_{f,j} \sum_{k=1}^{\infty} (-1)^k J_k \left(\frac{\Omega_\mu}{\omega_\mu}\right) [e^{-i(\Delta_q - k\omega_\mu)t} \bar{S}_{+,j} \sigma_- \\ & + \text{H.c.}] + \sum_j g_{f,j} J_0 \left(\frac{\Omega_\mu}{\omega_\mu}\right) [e^{-i\Delta_q t} \bar{S}_{+,j} \sigma_- + \text{H.c.}], \end{aligned} \quad (\text{A34})$$

with $\bar{S}_{+,j} = |e_j\rangle \langle 0_j|$ and $\bar{S}_{-,j} = \bar{S}_{+,j}^\dagger$. $\bar{\Delta}_q = \Delta_q - \omega_\mu$ and we set $\Delta_q \approx 700$ MHz. With this we can safely neglect the off-resonance terms for $k \neq 1$ and obtain the Hamiltonian

$$\begin{aligned} \hat{H} = & \frac{\dot{\phi}}{2} \sigma_z - \sum_j (\Delta_1 + \Delta_j - \delta_j - \dot{\phi}) |e_j\rangle \langle e_j| \\ & - \sum_j (\Delta_0 + \Delta_j) |0_j\rangle \langle 0_j| + \sum_j \Omega_c (|e_j\rangle \langle r_j| + |r_j\rangle \langle e_j|) \\ & + \sum_j (g_{c,j} e^{ikR_j} \hat{a}_j^\dagger |0_j\rangle \langle r_j| + g_{c,j} e^{-ikR_j} \hat{a} |r_j\rangle \langle 0_j|) \\ & - \sum_j g_{f,j} J_1 \left(\frac{\Omega_\mu}{\omega_\mu}\right) (e^{-i\bar{\Delta}_q t} \bar{S}_{+,j} \sigma_- + e^{i\bar{\Delta}_q t} \bar{S}_{-,j} \sigma_+). \end{aligned} \quad (\text{A35})$$

TABLE IX. Parameters of the flux qubit for our fit in Fig. 10.

$\gamma_{1,qb}/2\pi$ (MHz) decay rate of qubit	$\gamma_{2,qb}^*/2\pi$ (MHz) pure dephasing of qubit	$\Delta/2\pi$ (MHz) detuning
0.4	1.0	5.8 = $-E$ (Table II)

TABLE X. Parameters of the NV centers for our fit in Fig. 10.

$\bar{D}/2\pi$ (GHz)	$B_{z,j}$ (mT)	$E/2\pi$ (MHz)	$\Gamma_{1,en}/2\pi$ (MHz)	$\Gamma_{2,en}^*/2\pi$ (MHz) (pure dephasing)	N_g groups	$(D_+ - D_-)/2\pi$ (MHz)	N	$g_f/2\pi$ (MHz) grouped coupling	$\bar{g}_i/2\pi = \sqrt{N}g_i/2\pi$ (MHz)
2.878	0	Neglected	12	0.9	20	~ 0	1.6×10^7	5.56	35

In the optical dispersive Raman transition, we can adiabatically eliminate the states $|r_j\rangle$ [44], and the Hamiltonian becomes

$$\begin{aligned} \hat{H}_{\text{eff}} = & \frac{\dot{\phi} + \tilde{\Delta}_q}{2} \sigma_z - \sum_j \left[\Delta_1 + \Delta_j - \delta_j - \dot{\phi} \right. \\ & + \frac{\Omega_c^2(\Delta_1 + \Delta_j - \delta_j)}{(\Delta_1 + \Delta_j - \delta_j)^2 + (\gamma_j/2)^2} |e_j\rangle\langle e_j| \\ & - \sum_j \left[\Delta_0 + \Delta_j + \frac{g_{c,j}^2 \hat{a}^\dagger \hat{a} (\Delta_0 + \Delta_j)}{(\Delta_0 + \Delta_j)^2 + (\gamma_j/2)^2} \right] |g_j\rangle\langle g_j| \\ & - \sum_j g_{f,j} J_1 \left(\frac{\Omega_\mu}{\omega_\mu} \right) (\bar{S}_{+,j} \sigma_- + \bar{S}_{-,j} \sigma_+) \\ & - \frac{\Omega_c}{2} \sum_j g_{c,j} e^{ikR_j} \left(\frac{1}{\Delta_0 + \Delta_j - i\gamma_j/2} \right. \\ & \left. + \frac{1}{\Delta_0 + \Delta_j + i\gamma_j/2} \right) \hat{a}^\dagger |g_j\rangle\langle e_j| + \text{H.c.} \end{aligned} \quad (\text{A36})$$

We define $\Lambda_j = \frac{\Omega_c}{2} \bar{g}_c \left(\frac{1}{\Delta_0 + \Delta_j - i\gamma_j/2} + \frac{1}{\Delta_0 + \Delta_j + i\gamma_j/2} \right)$, $\xi_j = \frac{g_{c,j}}{\bar{g}_c}$ with $\bar{g}_c = \langle g_{c,j} \rangle$, $\theta_j = kR_j$. We also have the modified Lindblad operators from the decay channels $|r_j\rangle \rightarrow |g(e)_j\rangle$ as [44]

$$\begin{aligned} \hat{L}_{\text{eff},j}^{(0)} = & \frac{\sqrt{\gamma_{0,j}} g_{c,j} e^{-i\theta_j} \hat{a}}{(\Delta_0 + \Delta_j) + i\gamma_j/2} |g_j\rangle\langle g_j| \\ & + \frac{\sqrt{\gamma_{0,j}} \Omega_c}{(\Delta_0 + \Delta_j - \delta_j) - i\gamma_j/2} |g_j\rangle\langle e_j|, \end{aligned} \quad (\text{A37})$$

$$\begin{aligned} \hat{L}_{\text{eff},j}^{(1)} = & \frac{\sqrt{\gamma_{1,j}} g_{c,j} e^{-i\theta_j} \hat{a}}{(\Delta_0 + \Delta_j) + i\gamma_j/2} |e_j\rangle\langle g_j| \\ & + \frac{\sqrt{\gamma_{1,j}} \Omega_c}{(\Delta_0 + \Delta_j - \delta_j) - i\gamma_j/2} |e_j\rangle\langle e_j|. \end{aligned} \quad (\text{A38})$$

These operators will be later used for the swap and quantum transfer of quantum state.

If $|\Delta_0|, |\Delta_1| \gg \gamma_j, |\delta_j|$, we have

$$\begin{aligned} \hat{H}_{\text{eff}} = & \frac{\dot{\phi} + \tilde{\Delta}_q}{2} \sigma_z - \sum_j \hat{\Delta}_{\text{NV},j} |e_j\rangle\langle e_j| \\ & - \sum_j \left[\Delta_0 + \Delta_j + \frac{g_{c,j}^2 \hat{a}^\dagger \hat{a}}{(\Delta_0 + \Delta_j)} \right] |g_j\rangle\langle g_j| \end{aligned}$$

$$\begin{aligned} & - \sum_j g_{f,j} J_1 \left(\frac{\Omega_\mu}{\omega_\mu} \right) (\bar{S}_{+,j} \sigma_- + \bar{S}_{-,j} \sigma_+) \\ & - \sum_j \Lambda_j \xi_j \left(e^{i\theta_j} \hat{a}^\dagger \bar{S}_{-,j} + e^{-i\theta_j} \bar{S}_{+,j} \hat{a} \right), \end{aligned} \quad (\text{A39})$$

with $\hat{\Delta}_{\text{NV},j} = \Delta_1 + \Delta_j - \delta_j - \dot{\phi} + \frac{\Omega_c^2}{(\Delta_1 + \Delta_j - \delta_j)}$, $\Lambda_j = \frac{\Omega_c}{2} \bar{g}_c \left(\frac{1}{\Delta_0 + \Delta_j} + \frac{1}{\Delta_1 + \Delta_j - \delta_j} \right) \sim \frac{\Omega_c \bar{g}_c}{\Delta_0 + \Delta_j}$ because $\delta = \bar{D}$. If $|\Delta_0| \gg |\Delta_j|$, $\Lambda_j \approx \Lambda = \frac{\Omega_c \bar{g}_c}{\Delta_0}$ is constant in time. In our sideband transition regime, all parameters $\Omega_c, \Omega_\mu, \dot{\phi}, \tilde{\Delta}_q$ can be modulated in time. This flexibility provides a significant advantage over the fixed on-resonance coupling for transferring quantum information. When $\Omega_\mu = 1.8\omega_\mu$, the effective coupling between the flux qubit and the NV⁻ centers has maximum value $J_1(\Omega_\mu/\omega_\mu)g_{f,j} = 0.58g_{f,j}$. Note that the total coupling strength $\Lambda_{\text{tot}} = \frac{\sqrt{N} \bar{g}_c \Omega_c}{\Delta_0} = \frac{\sqrt{N} \bar{g}_c}{\Delta_0/\Omega_c}$ is the collective JC coupling strength which is suppressed by a factor of Δ_0/Ω_c in comparison with the on-resonance coupling rate $\sqrt{N} \bar{g}_c$.

b. Operators in the one-excitation space

In the OES including the cavity mode, we write the basis vectors ($N+3$ long, N the number of spins in the ensemble) as

$$\begin{aligned} |g_f, 0, G\rangle &= |g_f, 0, g_1, g_2, \dots, g_N\rangle = |0\rangle_M, \\ |e_f, 0, G\rangle &= |e_f, 0, g_1, g_2, \dots, g_N\rangle = |1\rangle_M, \\ |g_f, 1_c, G\rangle &= |g_f, 1_c, g_1, g_2, \dots, g_N\rangle = |2\rangle_M, \\ |g_f, 0, \dot{e}_j\rangle &= |g_f, 0, g_1, g_2, \dots, g_{j-1}, e_j, g_{j+1}, \dots, g_N\rangle \\ &= |j+2\rangle_M, \quad j = 1, 2, \dots, N. \end{aligned}$$

After defining the unitary operator for the system

$$\begin{aligned} \mathbb{I} = & \sum_{l=0}^{N+2} |l\rangle_M \langle l| \\ = & |g_f, 0, G\rangle\langle g_f, 0, G| + |e_f, 0, G\rangle\langle e_f, 0, G| \\ & + |g_f, 1_c, G\rangle\langle g_f, 1_c, G| + \sum_{j=1}^N |g_f, 0, \dot{e}_j\rangle\langle g_f, 0, \dot{e}_j|, \end{aligned}$$

the operators have the forms

$$\sigma_z = 2|1\rangle_M \langle 1| - \mathbb{I}, \quad (\text{A40a})$$

$$\sigma_+ = |e_f\rangle\langle e_f| = |1\rangle_M \langle 0|, \quad (\text{A40b})$$

$$\bar{S}_{z,j} = 2|j+2\rangle_M \langle j+2| - \mathbb{I}, \quad (\text{A40c})$$

TABLE XI. Variance in parameters for our fit in Fig. 10.

$\sigma_\delta/2\pi$ (MHz) (Variance in D_j of NVs)	$\sigma_{\Gamma_1}/\Gamma_{1,en}$ (Variance in decay rate of NVs)	$\sigma_{\Gamma_{2,en}}/\Gamma_{2,en}$ (Variance in decay rate of NVs)	σ_{g_f}/g_f (Variance in coupling between qubit and NVs)
14.4	0	10%	1%

$$\bar{S}_{+,j} = |j+2\rangle_M \langle 0|, \quad (\text{A40d})$$

$$\hat{a} = |0_c\rangle \langle 1_c| = |0\rangle_M \langle 2|, \quad (\text{A40e})$$

$$\hat{a}^\dagger \hat{a} = |1_c\rangle \langle 1_c| = |2\rangle_M \langle 2|. \quad (\text{A40f})$$

In the single-excitation basis, we have the relations $\sigma_z = 2\sigma_+\sigma_- = 2|1\rangle_M \langle 1|$ and $\bar{S}_{z,j} = 2\bar{S}_{+,j}\bar{S}_{-,j} = 2|j+2\rangle_M \langle j+2|$. So, the operators in the effective Hamiltonian above are given by

$$\hat{a}^\dagger \hat{a} |g_j\rangle \langle g_j| = |2\rangle_M \langle 2| = \hat{a}^\dagger \hat{a}, \quad (\text{A41a})$$

$$|\dot{e}_j\rangle \langle \dot{e}_j| = \bar{S}_{+,j} \bar{S}_{-,j}, \quad (\text{A41b})$$

$$|g_j\rangle \langle g_j| = (|g_j\rangle \langle g_j| + |e_j\rangle \langle e_j| - |e_j\rangle \langle e_j|) \quad (\text{A41c})$$

$$= \mathbb{I} - |g_f, 0_c, \dot{e}_j\rangle \langle g_f, 0_c, \dot{e}_j|$$

$$= \mathbb{I} - |j+2\rangle_M \langle j+2|,$$

$$\hat{a}^\dagger \hat{a} |e_j\rangle \langle e_j| = \emptyset. \quad (\text{A41d})$$

c. Master equation

Substituting Eqs. (A40) and (A41) into the effective Hamiltonian, \hat{H}_{eff} has the form

$$\begin{aligned} \hat{H}_{\text{eff}} = & (\dot{\phi} + \tilde{\Delta}_q) \sigma_+ \sigma_- - \sum_j \hat{\Delta}_{\text{NV},j} \bar{S}_{+,j} \bar{S}_{-,j} - \delta_{en} \hat{a}^\dagger \hat{a} \\ & - \sum_j g_{f,j} J_1 \left(\frac{\Omega_\mu}{\omega_\mu} \right) (\bar{S}_{+,j} \sigma_- + \bar{S}_{-,j} \sigma_+) \\ & - \sum_j \Lambda_j \xi_j (e^{i\theta_j} \hat{a}^\dagger \bar{S}_{-,j} + e^{-i\theta_j} \bar{S}_{+,j} \hat{a}), \end{aligned} \quad (\text{A42})$$

with $\delta_{en} = \sum_j \frac{g_{c,j}^2}{(\Delta_0 + \Delta_j)}$ is constant in time. Note that $g_{f,j}$, ξ_j , and θ_j are also constant. We modulate Ω_μ , $\dot{\phi}$, Ω_c , and ω_q , and subsequently Λ_j and $\tilde{\Delta}_q$ become time dependent. The full effective Hamiltonian in the OES in matrix form reads as

$$\hat{H}_{\text{eff}} = \begin{pmatrix} |g_f, 0, G\rangle & |e_f, 0, G\rangle & |g_f, 1, G\rangle & |g_f, 0, \dot{e}_1\rangle & |g_f, 0, \dot{e}_2\rangle & \dots & |g_f, 0, \dot{e}_N\rangle \\ |g_f, 0, G\rangle & 0 & 0 & 0 & 0 & \dots & 0 \\ |e_f, 0, G\rangle & 0 & (\dot{\phi} + \tilde{\Delta}_q) & 0 & -g_{f,2} J_1 \left(\frac{\Omega_\mu}{\omega_\mu} \right) & \dots & -g_{f,N} J_1 \left(\frac{\Omega_\mu}{\omega_\mu} \right) \\ |g_f, 1, G\rangle & 0 & 0 & -\delta_{en} & -\Lambda_1 \xi_1 e^{i\theta_1} & -\Lambda_2 \xi_2 e^{i\theta_2} & \dots & -\Lambda_N \xi_N e^{i\theta_N} \\ |g_f, 0, \dot{e}_1\rangle & 0 & -g_{f,1} J_1 \left(\frac{\Omega_\mu}{\omega_\mu} \right) & -\Lambda_1 \xi_1 e^{-i\theta_1} & -\hat{\Delta}_{\text{NV},1} & 0 & \dots & 0 \\ |g_f, 0, \dot{e}_2\rangle & 0 & -g_{f,2} J_1 \left(\frac{\Omega_\mu}{\omega_\mu} \right) & -\Lambda_2 \xi_2 e^{-i\theta_2} & 0 & -\hat{\Delta}_{\text{NV},2} & \dots & 0 \\ \vdots & \vdots & \vdots & \vdots & \vdots & \vdots & \ddots & \vdots \\ |g_f, 0, \dot{e}_N\rangle & 0 & -g_{f,N} J_1 \left(\frac{\Omega_\mu}{\omega_\mu} \right) & -\Lambda_N \xi_N e^{-i\theta_N} & 0 & 0 & \dots & -\hat{\Delta}_{\text{NV},N} \end{pmatrix}. \quad (\text{A43})$$

The superoperators describing the dissipation and pure dephasing for all systems are

$$\mathcal{L}_q^{(1)}[\rho] = \frac{\gamma_{1,qb}}{2} (2\sigma_- \rho \sigma_+ - \sigma_+ \sigma_- \rho - \rho \sigma_+ \sigma_-),$$

$$\mathcal{L}_q^{(2)}[\rho] = \gamma_{2,qb}^* (\sigma_z \rho \sigma_z - \rho),$$

$$\mathcal{L}_{\text{NV},j}^{(1)}[\rho] = \frac{\Gamma_{1,j}}{2} (2\bar{S}_{-,j} \rho \bar{S}_{+,j} - \bar{S}_{+,j} \bar{S}_{-,j} \rho - \rho \bar{S}_{+,j} \bar{S}_{-,j}),$$

$$\mathcal{L}_{\text{NV},j}^{(2)}[\rho] = \Gamma_{2,j}^* (\bar{S}_{z,j} \rho \bar{S}_{z,j} - \rho),$$

$$\mathcal{L}_c[\rho] = \frac{\kappa}{2} (2\hat{a} \rho \hat{a}^\dagger - \hat{a}^\dagger \hat{a} \rho - \rho \hat{a}^\dagger \hat{a}),$$

$$\begin{aligned} \mathcal{L}_{\text{NV},j}^{(L_0)}[\rho] = & \frac{1}{2} (2\hat{L}_{\text{eff},j}^{(0)} \rho \hat{L}_{\text{eff},j}^{(0)\dagger} - \hat{L}_{\text{eff},j}^{(0)\dagger} \hat{L}_{\text{eff},j}^{(0)} \rho \\ & - \rho \hat{L}_{\text{eff},j}^{(0)\dagger} \hat{L}_{\text{eff},j}^{(0)}), \end{aligned}$$

$$\begin{aligned} \mathcal{L}_{\text{NV},j}^{(L_1)}[\rho] = & \frac{1}{2} (2\hat{L}_{\text{eff},j}^{(1)} \rho \hat{L}_{\text{eff},j}^{(1)\dagger} - \hat{L}_{\text{eff},j}^{(1)\dagger} \hat{L}_{\text{eff},j}^{(1)} \rho \\ & - \rho \hat{L}_{\text{eff},j}^{(1)\dagger} \hat{L}_{\text{eff},j}^{(1)}). \end{aligned}$$

Thus, the dynamics of the node can be described by the Lindblad master equation

$$\begin{aligned} \frac{\partial \rho}{\partial t} = & -i[\hat{H}_{\text{eff}}, \rho] + \mathcal{L}_q^{(1)}[\rho] + \mathcal{L}_q^{(2)}[\rho] + \mathcal{L}_c[\rho] \\ & + \sum_j \mathcal{L}_{\text{NV},j}^{(1)}[\rho] + \sum_j \mathcal{L}_{\text{NV},j}^{(2)}[\rho] \\ & + \sum_j \mathcal{L}_{\text{NV},j}^{(L_0)}[\rho] + \sum_j \mathcal{L}_{\text{NV},j}^{(L_1)}[\rho]. \end{aligned} \quad (\text{A44})$$

d. MQ-Optical swap quantum state via STIRAP

We are interested in the transfer of quantum state between the flux qubit and optical mode using the STIRAP method because it is robust against the imperfection in the control process [45] and avoids much excitation of the spins. We now assume the tripartite two-level (2L) system interacts on resonance, i.e., under the one-photon resonance condition (OPRC). To enable the OPRC, the spin ensemble must interact on resonance with the photon in the optical mode and also with the first sideband transition of the flux qubit. Thus, we have

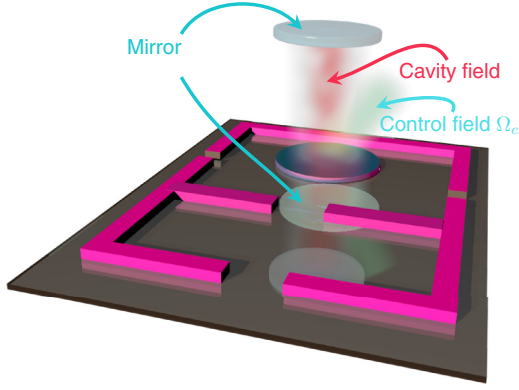


FIG. 11. (Color online) Schematic diagram of the interaction among the hybrid quantum system consisting of a flux qubit, an ensemble of spins, and an optical cavity.

the relations

$$\dot{\phi} = \Delta_1 - \Delta_0 + \frac{\Omega_c^2}{\Delta_1} - \delta_{en} \text{ (NVs-photons)}, \quad (\text{A45})$$

$$\dot{\phi} + \tilde{\Delta}_q = -\delta_{en} \text{ (qubit-NVs)} \quad (\text{A46})$$

yielding

$$\dot{\phi} = \Delta_1 - \Delta_0 + \frac{\Omega_c^2}{\Delta_1} - \delta_{en}, \quad (\text{A47})$$

$$\omega_q = \omega_\mu + \bar{D} - \frac{\Omega_c^2}{\Delta_1}, \quad (\text{A48})$$

$$\omega_\mu = \Delta_q + \delta_{en} + \dot{\phi}. \quad (\text{A49})$$

Using Gaussian control paired pulses $J_1(\Omega_\mu/\omega_\mu) = 0.58e^{-(t-\tau_{d,f})^2/2\tau_f^2}$ and $\Omega_c = \Omega_{c,0}e^{-(t-\tau_{d,c})^2/2\tau_c^2}$ with the amplitude $\Omega_{c,0}$ of the coherent control field, we can swap the quantum state from the flux qubit to the cavity mode with a fidelity $\mathcal{F} = \sqrt{\langle \psi | \rho | \psi \rangle}$ [46] larger than 90% (see Fig. 13). We also calculate the fidelity shown in Figs. 13(b) and 13(c) as a function of the decay rate κ of the cavity and the coupling rate g_f and the optical Raman transition rate $\Lambda_R \sim \frac{\Omega_c g_c}{\Delta_0}$ by setting $g = 0.58\sqrt{N}\langle g_{f,j} \rangle = \Lambda_R$. During the scan, we fix the pulse widths $g\tau_f = g\tau_c = 2.1$ and delays $\tau_{d,f} - \tau_{d,c} = 1.25\tau_f$ for $\gamma_{1,qb} = 0.4$ MHz in Fig. 13(b), while $g\tau_f = g\tau_c = 6.3$ and $\tau_{d,f} - \tau_{d,c} = 1.2\tau_f$ for $\gamma_{1,qb} = 0.02$ MHz in Fig. 13(c). For a flux-qubit decay rate $\gamma_{1,qb} = 0.4$ MHz, we can achieve a swap fidelity larger than 0.81 if $\kappa \leq 5\gamma_{1,qb}$ and $g > 40$ MHz. This shows that if the qubit and cavity decay quickly, then to achieve the transfer fast enough to avoid significant loss, then the coupling to the spin ensemble must be quite large. However, practically the magnitude of this coupling g can be much reduced if the qubit and the cavity decay more slowly. As shown in Fig. 13(c), the fidelity can be higher than 73% for $\gamma_{1,qb} = 20$ kHz, $\kappa \leq 5\gamma_{1,qb}$ and $g > 10$ MHz corresponding to a collective coupling strength $\sqrt{N}\langle g_{f,j} \rangle > 18$ MHz. Such high-quality flux qubits [21,22] and Fabry-Pérot cavities [23] are available using existing experimental technology.

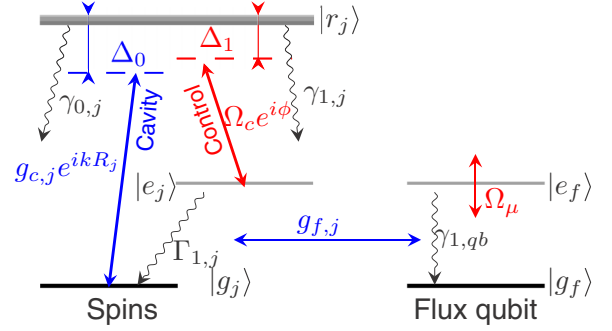


FIG. 12. (Color online) Level diagram showing the interactions between spins (left panel) and optical fields ($g_{c,j}e^{ikR_j}$ for the cavity mode and $\Omega_c e^{i\phi}$ for the classical driving) and qubit (right panel). The energy of levels $|r_j\rangle$ and $|e_j\rangle$ of the spins have an inhomogeneous broadening of Δ_j and δ_j , respectively. The inhomogeneity in the phase $\phi(t)$ is absorbed into ikR_j which is dependent on the site of the spin R_j . The occupation in the state $|r_j\rangle$ decays to the state $|e_j\rangle$ and $|g_j\rangle$ with rates $\gamma_{1,j}$ and $\gamma_{0,j}$, respectively. $\gamma_j = \gamma_{0,j} + \gamma_{1,j}$ is the total dissipation rate of $|r_j\rangle$. The state $|e_j\rangle$ also decays to the state $|g_j\rangle$ with a rate $\Gamma_{1,j}$ due to the magnetic dipole transition. $\gamma_{1,q}$ is the dissipation rate of the flux qubit whose transition frequency is modulated with amplitude Ω_μ and frequency ω_μ . The qubit-spin coupling rate is $g_{f,j}$.

3. Remote quantum transfer

To construct a quantum network, we create a tripartite Raman transition in each node, as shown in Fig. 14. We now

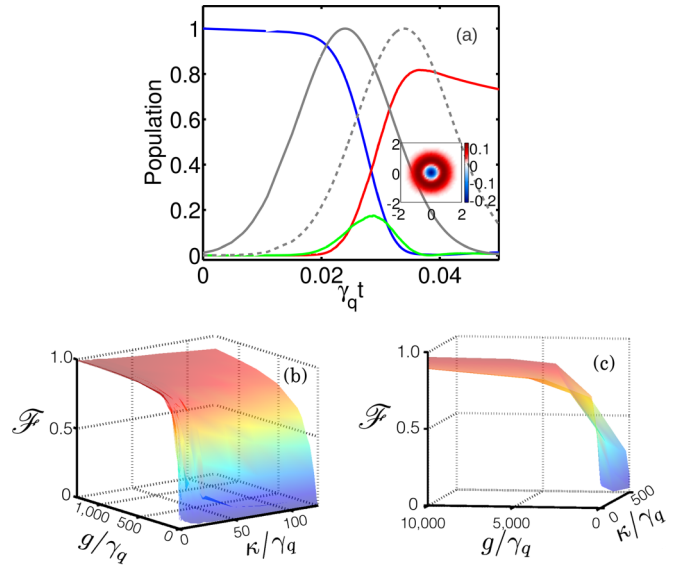


FIG. 13. (Color online) Swap of quantum information from the flux qubit to the cavity mode via the STIRAP protocol. (a) Gray lines are the time-modulated STIRAP couplings via a driving classical optical field $\Omega_c(t)$ (solid line) and modulated cavity-QED coupling strength $g_f J_1[\Omega_\mu(t)/\omega_\mu]$ (dashed line). Blue line shows the population of the excited state of the source flux qubit, red line is the population of the target photonic state $|n=1\rangle$, while green line shows collective excitation of the spins. Inset is the Wigner function of the cavity mode at $\gamma_{1,qb}t = 0.036$. We have chosen parameter values such that $\gamma_{1,qb} = 0.4$ MHz, $\kappa = 3$ MHz, and $g = 105$ MHz. Subplots (b) and (c) show the swap fidelity as a function of κ and g for $\gamma_{1,qb} = 0.4$ MHz (b) and (c) with $\gamma_{1,qb} = 0.02$ MHz.

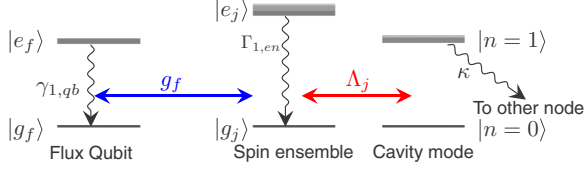


FIG. 14. (Color online) Schematic diagram for the tripartite Raman transition in one node.

consider that the ensemble of spins dispersively couples to the flux qubit and the cavity mode. The photon from the cavity is injected into an optical fiber and is then received by the cavity in another node. To transfer the quantum information between two distant nodes, we modulate the coupling rate $\Lambda_j(t)$ by tuning the coherent control field $\Omega_c(t)$, remembering that the flux qubit couples to the spins with constant rates $g_{f,j}$.

The Hamiltonian describing the motion of the system in each node is given by Eq. (A42) in the sideband transition regime. However, to build a quantum internet, we do not need to modulate the coupling g_f because we can quickly adjust the coherent optical driving Ω_c , which in turn will modulate the overall microwave-optical coupling strength. With this, the flux qubit can interact resonantly with the spins with a constant

coupling rate if needed. The Hamiltonian is given by

$$\begin{aligned} \hat{H}_{\text{eff}} = & (\dot{\phi} + \Delta_q)\sigma_+\sigma_- - \sum_j \hat{\Delta}_j \bar{S}_{+,j} \bar{S}_{-,j} - \delta_{en} \hat{a}^\dagger \hat{a} \\ & - \sum_j g_{f,j} (\bar{S}_{+,j} \sigma_- + \bar{S}_{-,j} \sigma_+) \\ & - \sum_j \Lambda_j(t) \xi_j (e^{i\theta_j} \hat{a}^\dagger \bar{S}_{-,j} + e^{-i\theta_j} \bar{S}_{+,j} \hat{a}). \end{aligned} \quad (\text{A50})$$

In this arrangement, the flux qubit can interact resonantly with the spins with a constantly maximal coupling rate if needed. In comparison with the case modulating the qubit-spin coupling but fixing the spin-cavity coupling, it allows us to transfer quantum information with a faster speed and a higher fidelity.

a. Two-node quantum network in the one-excitation space

Now, we study the simplest quantum network with two nodes A and B , each node including N_A (N_B) NV centers (see Fig. 15). Although their individual OES basis span a Hilbert space, they share a common ground state. Again, in the OES we have the basis

$$|g_f, 0, G; g_f, 0, G\rangle = |g_f, 0, g_1, g_2, \dots, g_{N_A}; g_f, 0, g_1, g_2, \dots, g_{N_B}\rangle = |0\rangle_M, \quad (\text{A51a})$$

$$|e_f, 0, G\rangle_A = |e_f, 0, g_1, g_2, \dots, g_{N_A}; g_f, 0, g_1, g_2, \dots, g_{N_B}\rangle = |1\rangle_M, \quad (\text{A51b})$$

$$|g_f, 1_c, G\rangle_A = |g_f, 1_c, g_1, g_2, \dots, g_{N_A}; g_f, 0, g_1, g_2, \dots, g_{N_B}\rangle = |2\rangle_M, \quad (\text{A51c})$$

$$|g_f, 0, \dot{e}_j\rangle_A = |g_f, 0, g_1, g_2, \dots, g_{j-1}, e_j, g_{j+1}, \dots, g_{N_A}; g_f, 0, g_1, g_2, \dots, g_{N_B}\rangle = |j+2\rangle_M, \quad j = 1, 2, \dots, N_A \quad (\text{A51d})$$

$$|e_f, 0, G\rangle_B = |g_f, 0, g_1, g_2, \dots, g_{N_A}; e_f, 0, g_1, g_2, \dots, g_{N_B}\rangle = |N_A + 3\rangle_M, \quad (\text{A51e})$$

$$|g_f, 1_c, G\rangle_B = |g_f, 0, g_1, g_2, \dots, g_{N_A}; g_f, 1_c, g_1, g_2, \dots, g_{N_B}\rangle = |N_A + 4\rangle_M, \quad (\text{A51f})$$

$$|g_f, 0, \dot{e}_j\rangle_B = |g_f, 0, g_1, g_2, \dots, g_{N_A}; g_f, 0, g_1, g_2, \dots, g_{j-1}, e_j, g_{j+1}, \dots, g_{N_B}\rangle = |j + N_A + 4\rangle_M, \quad j = 1, 2, \dots, N_B. \quad (\text{A51g})$$

The size of this OES is $M = N_A + N_B + 5$. We define the identity operator for the whole system

$$\begin{aligned} \mathbb{I}_{\text{Net}} = & \sum_{l=0}^{N_A+N_B+4} |l\rangle_M \langle l| \\ = & |g_f, 0, G\rangle_A \langle g_f, 0, G| + |e_f, 0, G\rangle_A \langle e_f, 0, G| \\ & + |g_f, 1_c, G\rangle_A \langle g_f, 1_c, G| + \sum_{j=1}^N |g_f, 0, \dot{e}_j\rangle_A \langle g_f, 0, \dot{e}_j| \\ & + |g_f, 0, G\rangle_B \langle g_f, 0, G| + |e_f, 0, G\rangle_B \langle e_f, 0, G| \\ & + |g_f, 1_c, G\rangle_B \langle g_f, 1_c, G| + \sum_{j=1}^N |g_f, 0, \dot{e}_j\rangle_B \langle g_f, 0, \dot{e}_j|. \end{aligned} \quad (\text{A52})$$

Then, the relevant operators have the forms

$$\sigma_{+,A} = |1\rangle_M \langle 0|, \quad (\text{A53a})$$

$$\sigma_{z,A} = 2\sigma_{+,A}\sigma_{-,A}, \quad (\text{A53b})$$

$$\bar{S}_{+,A} = |j+2\rangle_M \langle 0|, \quad j = 1, 2, \dots, N_A \quad (\text{A53c})$$

$$\bar{S}_{z,A} = 2\bar{S}_{+,A}\bar{S}_{-,A}, \quad (\text{A53d})$$

$$|e_j\rangle_A \langle e_j| = \bar{S}_{+,A}\bar{S}_{-,A}, \quad (\text{A53e})$$

$$|0_j\rangle_A \langle 0_j| = \mathbb{I}_{\text{Net}} - \bar{S}_{+,A}\bar{S}_{-,A}, \quad (\text{A53f})$$

$$\sigma_{+,B} = |N_A + 3\rangle_M \langle 0|, \quad (\text{A53g})$$

$$\sigma_{z,A} = 2\sigma_{+,A}\sigma_{-,A}, \quad (\text{A53h})$$

$$\bar{S}_{+,B} = |j + N_A + 4\rangle_M \langle 0|, \quad j = 1, 2, \dots, N_B \quad (\text{A53i})$$

$$\bar{S}_{z,B} = 2\bar{S}_{+,B}\bar{S}_{-,B}, \quad (\text{A53j})$$

$$|e_j\rangle_B \langle e_j| = \bar{S}_{+,B}\bar{S}_{-,B}, \quad (\text{A53k})$$

$$|0_j\rangle_B \langle 0_j| = \mathbb{I}_{\text{Net}} - \bar{S}_{+,B}\bar{S}_{-,B}, \quad (\text{A53l})$$

$$\hat{a}_A = |0\rangle_M \langle 2|, \quad (\text{A53m})$$

$$\hat{a}_B = |0\rangle_M \langle 4|. \quad (\text{A53n})$$

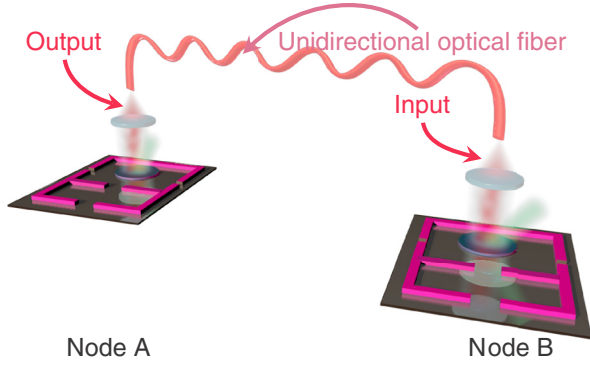


FIG. 15. (Color online) Schematic diagram for a two-node quantum network. The quantum information of the node A (left) is sent to the node B (right) via a unidirectional optical fiber (red curve). Here, we neglect the optical circulator.

Using the basis and operators above, we can extend the effective Hamiltonian and master equation into a two-node quantum network if a connecting unidirectional cascaded Lindblad operator is provided as follows:

$$\hat{L}_{\text{Net}} = -\sqrt{\kappa_{ex,A}\kappa_{ex,B}}(\hat{a}_B^\dagger \hat{a}_A \rho - \hat{a}_A \rho \hat{a}_B^\dagger + \rho \hat{a}_A^\dagger \hat{a}_B - \hat{a}_B \rho \hat{a}_A^\dagger), \quad (\text{A54})$$

where $\kappa_{ex,A/B}$ is the decay rate of cavities A and B due to the external coupling to a quantum bus, e.g., optical fibers.

b. Tripartite Raman transition

To transfer quantum state between two distant superconducting qubits using the 1997PhRvL..78.3221C scheme [14], we need to adiabatically eliminate the spins. To achieve this, the flux qubit and the cavity must dispersively couple to the spins and together they form a tripartite Raman transition under the tripartite two-photon resonance conditions

$$\dot{\phi} = \Delta_1 - \Delta_0 + \frac{\Omega_c^2}{\Delta_1} - \delta_{en} - \Delta_{SP} \quad (\text{NVs-photons}), \quad (\text{A55})$$

$$\dot{\phi} + \tilde{\Delta}_q = -\delta_{en} \quad (\text{qubit-NVs}), \quad (\text{A56})$$

where Δ_{SP} is the one-photon detuning between the spins and the flux qubit and the cavity. Thus, we have

$$\dot{\phi} = \Delta_1 - \Delta_0 + \frac{\Omega_c^2}{\Delta_1} - \delta_{en} - \Delta_{SP}, \quad (\text{A57})$$

$$\begin{aligned} \omega_\mu &= \Delta_q + \delta_{en} + \dot{\phi} \\ &= (\Delta_1 - \Delta_0) + \frac{\Omega_c^2}{\Delta_1} - \Delta_{SP} + \Delta_q. \end{aligned} \quad (\text{A58})$$

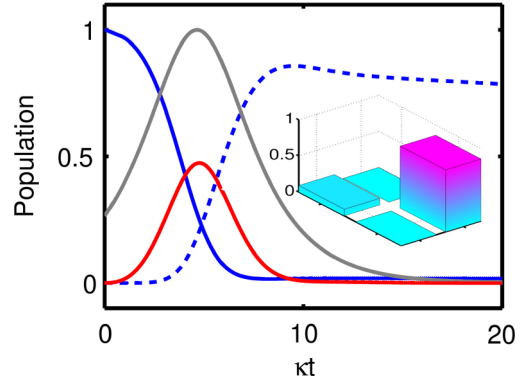


FIG. 16. (Color online) Quantum transfer from the flux qubit A to the qubit B . To perform the remote transfer of quantum information, the protocol requires identical and simultaneous controls in both A and B nodes if we eliminate the time delay due to the retardation in the propagation in optical fiber [14]. The chirp $\dot{\phi}$ and the detuning Δ_q are constant in time. Parameters are listed in Table XII. Black lines are the normalized modulated couplings, which are on top of each other. Solid (dashed) blue line shows the population of the excited state of the flux qubit A (B). Red line for the excitation of the antisymmetric state of the cavity mode. The inset bar is the density matrix of the flux qubit B at time $\kappa t = 9.35$.

Because Ω_c varies in time, the chirp $\dot{\phi}$ and Δ_q must also be modulated in time while Ω_c^2/Δ_1 is about few hundred of MHz. We apply the sech-function time modulation of the couplings with amplitude $\Omega_{c,0} = \sqrt{N} \bar{g}_c = 200\kappa$ and with detuning $\Delta_0 = \Delta_1 \gg \Omega_{c,0}$ [24]. For an easy implementation, we fix the chirp $\dot{\phi} = \Delta_1 - \Delta_0 + \frac{\Omega_{c,0}^2}{\Delta_1} - \delta_{en} - \Delta_{SP}$ and apply a constant detuning Δ_q . This arrangement only perfectly cancels the ac Stark shift at the peak of the coupling. However, the fidelity remains high, about 92.7% at $\kappa t = 9.35$, as shown in Fig. 16. We can further modulate the transition frequency ω_q of the flux qubits to tune Δ_q . This allows complete cancellation of the ac Stark shift over the whole optical driving period and result in a higher fidelity of transfer $F = 93\%$.

4. Parameter estimation

To predict the reasonable performance of our scheme, the best available parameters are crucial. Now, we turn to estimate the available optical coupling rates between the spins and the qubit and the photon.

First, we address the coupling rates for the ensemble of NV^- centers. The cavity mode optically drives the zero-phonon line of the NV^- centers. Thus, the resonance wavelength of a Fabry-Pérot cavity is about $\lambda_c \sim 637$ nm corresponding to the resonance frequency $\omega_c = 4.7 \times 10^{14}$ Hz and we assume the mode volume $V_c = 1000\lambda_c^3$. Thus, the zero-point fluctuation of electric field in the cavity can be evaluated to

TABLE XII. Parameters for simulations in Fig. 16.

κ (MHz)	$\sqrt{N} \bar{g}_c$	Ω_c	$\Delta_0 = \Delta_1$	σ_θ	$\gamma_{1,qb}$ (kHz)	$\gamma_{2,qb}^*$	Δ_q (MHz)	$\sqrt{N} \bar{g}_f$	$\Gamma_{1,en}$ (MHz)	$\Gamma_{2,en}^*$ (MHz)	σ_δ (MHz)	σ_Δ (MHz)	Δ_{SP}
10	200κ	$200\kappa \text{sech}[-(0.43\kappa t - 2)]$	$20\sqrt{N} \bar{g}_c$	0.1π	20	0	700	10κ	12	0.9	14.4	10	$20\sqrt{N} \bar{g}_f$

be $E_0 = \sqrt{\frac{\hbar\omega_c}{\epsilon_0 V_c}} = 1.1677 \times 10^4 \text{ V m}^{-1}$. The electric dipole moment of a NV^- center is about $\mu = 3.0 \times 10^{-29} \text{ C m}$ [47] yielding a single-photon coupling rate $g_c \approx 0.53 \text{ GHz}$ for a single NV center. An ensemble of $N = 3 \times 10^6$ NV^- centers ($\rho = 8 \times 10^{18} \text{ cm}^{-3}$) can generate a collective coupling rate $\sqrt{N}g_c \approx 2.9 \text{ THz}$, which is large enough for all investigation in our work. This large coupling rate can relax the optical experiment design. To achieve a uniform optical coupling to the cavity mode, the physical thickness of diamond chip t_{chip} must be much smaller than the optical resonance wavelength of the cavity. In our investigation, $t_{\text{chip}} < \lambda_c/8n_{\text{chip}}$ where n_{chip} is the refractive index of the host crystal chip. Unlike the quantum memory in [8], this thin diamond film limits the available magnetic coupling rate. According to Eq. (A9), the collective magnetic coupling rate is proportional to $\sqrt{N}B \approx I_p \sqrt{t_{\text{chip}}\rho}$ with the concentration of spins ρ . For the persistent current $I_p = 800 \text{ mA}$, $R_Q = 5.6 \mu\text{m}$ and $t_{\text{chip}} = 0.12\lambda_c/n_{\text{chip}}$ with $n_{\text{chip}} = 2$ for diamond, the maximal coupling rate $\sqrt{N}\bar{g}_f$ is about 19 MHz. However, we can increase the magnetic field by an order by using a flux focuser [26–28].

The relatively small magnetic coupling rate of the flux qubit to the NV^- centers embedded in a crystal chip of the above dimension limits the performance of our quantum interface for transferring quantum information. In contrast, if we instead use a chip of rare-earth crystal, the rare-earth ions enjoy a stronger coupling because they possess a much larger g factor. Following, we look into the coupling of rare-earth ions to the flux qubit. We assume that a cavity mode with resonance wavelength $\lambda_c \sim 1536 \text{ nm}$ and frequency $\omega_c = 1.95 \times 10^{14} \text{ Hz}$ drives the optical transition of Er^{3+} . The electric dipole moment of Er^{3+} is small, about $2.07 \times 10^{-32} \text{ C m}$ [48]. However, the concentration of rare-earth ions can be large [36]. Assuming that $n_{\text{chip}} = 1.8$ for $\text{Er}^{3+} : \text{Y}_2\text{SiO}_5$, $R_Q = 5.6 \mu\text{m}$, $t_{\text{chip}} \sim 0.1\lambda_c/n_{\text{chip}}$, and $\rho = 50 \times 10^{18} \text{ cm}^{-3}$ (0.25%) yielding $N = 4 \times 10^9$ allows a collective optical coupling rate of $2\pi \times 4 \text{ GHz}$, while the magnetic coupling rate can be $2\pi \times 370 \text{ MHz}$ for $I_p = 800 \text{ mA}$ and $R_Q = 17 \mu\text{m}$. In terms of the magnetic coupling, a rare-earth chip is considerably better than a diamond crystal chip.

-
- [1] M. H. Devoret and R. J. Schoelkopf, *Science* **339**, 1169 (2013).
 - [2] H. J. Kimble, *Nature (London)* **453**, 1023 (2008).
 - [3] B. Fröhlich, J. F. Dynes, M. Lucamarini, A. W. Sharpe, Z. Yuan, and A. J. Shields, *Nature (London)* **501**, 69 (2013).
 - [4] S. Ritter, C. Nölleke, C. Hahn, A. Reiserer, A. Neuzner, M. Uphoff, M. Mücke, E. Figueroa, J. Bochmann, and G. Rempe, *Nature (London)* **484**, 195 (2012).
 - [5] Y. Kubo, F. R. Ong, P. Bertet, D. Vion, V. Jacques, D. Zheng, A. Dreau, J. F. Roch, A. Auffeves, F. Jelezko, J. Wrachtrup, M. F. Barthe, P. Bergonzo, and D. Esteve, *Phys. Rev. Lett.* **105**, 140502 (2010).
 - [6] D. I. Schuster, A. P. Sears, E. Ginossar, L. DiCarlo, L. Frunzio, J. J. L. Morton, H. Wu, G. A. D. Briggs, B. B. Buckley, D. D. Awschalom, and R. J. Schoelkopf, *Phys. Rev. Lett.* **105**, 140501 (2010).
 - [7] P. Bushev, A. K. Feofanov, H. Rotzinger, I. Protopopov, J. H. Cole, C. M. Wilson, G. Fischer, A. Lukashenko, and A. V. Ustinov, *Phys. Rev. B* **84**, 060501 (2011).
 - [8] X. Zhu, S. Saito, A. Kemp, K. Kakuyanagi, S.-i. Karimoto, H. Nakano, W. J. Munro, Y. Tokura, M. S. Everitt, K. Nemoto, M. Kasu, N. Mizuochi, and K. Semba, *Nature (London)* **478**, 221 (2012).
 - [9] L. A. Williamson, Y.-H. Chen, and J. J. Longdell, *Phys. Rev. Lett.* **113**, 203601 (2014).
 - [10] C. O'Brien, N. Lauk, S. Blum, G. Morigi, and M. Fleischhauer, *Phys. Rev. Lett.* **113**, 063603 (2014).
 - [11] C. K. Andersen and K. Mølmer, *Phys. Rev. A* **86**, 043831 (2012).
 - [12] S. Saito, X. Zhu, R. Amsüss, Y. Matsuzaki, K. Kakuyanagi, T. Shimo-Oka, N. Mizuochi, K. Nemoto, W. J. Munro, and K. Semba, *Phys. Rev. Lett.* **111**, 107008 (2013).
 - [13] B. Julsgaard, C. Grezes, P. Bertet, and K. Mølmer, *Phys. Rev. Lett.* **110**, 250503 (2013).
 - [14] J. I. Cirac, P. Zoller, H. J. Kimble, and H. Mabuchi, *Phys. Rev. Lett.* **78**, 3221 (1997).
 - [15] K. Xia, G. Lu, G. Lin, Y. Cheng, Y. Niu, S. Gong, and J. Twamley, *Phys. Rev. A* **90**, 043802 (2014).
 - [16] V. M. Acosta, K. Jensen, C. Santori, D. Budker, and R. G. Beausoleil, *Phys. Rev. Lett.* **110**, 213605 (2013).
 - [17] E. Baldit, K. Bencheikh, P. Monnier, S. Briaudeau, J. A. Levenson, V. Crozatier, I. Lorgère, F. Bretenaker, J. L. Le Gouët, O. Guillot-Noël, and P. Goldner, *Phys. Rev. B* **81**, 144303 (2010).
 - [18] T. Böttger, C. W. Thiel, Y. Sun, and R. L. Cone, *Phys. Rev. B* **74**, 075107 (2006).
 - [19] B. Lauritzen, J. Minář, H. de Riedmatten, M. Afzelius, and N. Gisin, *Phys. Rev. A* **83**, 012318 (2011).
 - [20] F. Bussières, C. Clausen, A. Tiranov, B. Korzh, V. B. Verma, S. W. Nam, F. Marsili, A. Ferrier, P. Goldner, H. Herrmann, C. Silberhorn, W. Sohler, M. Afzelius, and N. Gisin, *Nat. Photonics* **8**, 775 (2014).
 - [21] J. Bylander, S. Gustavsson, F. Yan, F. Yoshihara, K. Harrabi, G. Fitch, D. G. Cory, Y. Nakamura, J.-S. Tsai, and W. D. Oliver, *Nat. Phys.* **7**, 565 (2011).
 - [22] A. Fedorov, A. K. Feofanov, P. Macha, P. Forn-Díaz, C. J. P. M. Harmans, and J. E. Mooij, *Phys. Rev. Lett.* **105**, 060503 (2010).
 - [23] W. Chen, K. M. Beck, R. Bücker, M. Gullans, M. D. Lukin, H. Tanji-Suzuki, and V. Vuletić, *Science* **341**, 768 (2013).
 - [24] T. M. Stace and C. H. W. Barnes, *Phys. Rev. A* **65**, 062308 (2002).
 - [25] S. Probst, H. Rotzinger, S. Wünsch, P. Jung, M. Jerger, M. Siegel, A. V. Ustinov, and P. A. Bushev, *Phys. Rev. Lett.* **110**, 157001 (2013).
 - [26] G. Lipworth, J. Ensworth, K. Seetharam, D. Huang, J. S. Lee, P. Schmalenberg, T. Nomura, M. S. Reynolds, D. R. Smith, and Y. Urzhumov, *Sci. Rep.* **4**, 3642 (2014).
 - [27] C. H. Wu, M. H. Hsu, K. L. Chen, J. C. Chen, J. T. Jeng, T. S. Lai, H.-E. Horng, and H.-C. Yang, *Supercond. Sci. Technol.* **19**, S246 (2006).

- [28] A. N. Matlashov, V. P. Koshelets, P. V. Kalashnikov, Y. E. Zhuravlev, V. Y. Slobodchikov, S. A. Kovtonyuk, and L. V. Filippenko, *IEEE Trans. Mag.* **27**, 2963 (1991).
- [29] T. P. Orlando, J. E. Mooij, L. Tian, C. H. van der Wal, L. S. Levitov, S. Lloyd, and J. J. Mazo, *Phys. Rev. B* **60**, 15398 (1999).
- [30] X. Zhu, A. Kemp, S. Saito, and K. Semba, *Appl. Phys. Lett.* **97**, 102503 (2010).
- [31] K. Xia, G. K. Brennen, D. Ellinas, and J. Twamley, *Opt. Express* **20**, 27198 (2012).
- [32] V. M. Acosta, A. Jarmola, E. Bauch, and D. Budker, *Phys. Rev. B* **82**, 201202 (2010).
- [33] J. R. Maze, A. Gali, E. Togan, Y. Chu, A. Trifonov, E. Kaxiras, and M. D. Lukin, *New J. Phys.* **13**, 025025 (2011).
- [34] K.-M. C. Fu, C. Santori, P. E. Barclay, L. J. Rogers, N. B. Manson, and R. G. Beausoleil, *Phys. Rev. Lett.* **103**, 256404 (2009).
- [35] Y. Sun, T. Böttger, C. W. Thiel, and R. L. Cone, *Phys. Rev. B* **77**, 085124 (2008).
- [36] A. Tkalc̃ec, S. Probst, D. Rieger, H. Rotzinger, S. Wünsch, N. Kukharchyk, A. D. Wieck, M. Siegel, A. V. Ustinov, and P. Bushev, *Phys. Rev. B* **90**, 075112 (2014).
- [37] Z. Kurucz, J. H. Wesenberg, and K. Mølmer, *Phys. Rev. A* **83**, 053852 (2011).
- [38] I. Diniz, S. Portolan, R. Ferreira, J. M. Gérard, P. Bertet, and A. Auffèves, *Phys. Rev. A* **84**, 063810 (2011).
- [39] K. Sandner, H. Ritsch, R. Amsüss, C. Koller, T. Nöbauer, S. Putz, J. Schmiedmayer, and J. Majer, *Phys. Rev. A* **85**, 053806 (2012).
- [40] J. D. Strand, M. Ware, F. Beaudoin, T. A. Ohki, B. R. Johnson, A. Blais, and B. L. T. Plourde, *Phys. Rev. B* **87**, 220505 (2013).
- [41] J. M. Pirkkalainen, S. U. Cho, J. Li, G. S. Paraoanu, P. J. Hakonen, and M. A. Sillanpää, *Nature (London)* **494**, 211 (2013).
- [42] I. Chiorescu, P. Bertet, K. Semba, Y. Nakamura, C. J. P. M. Harmans, and J. E. Mooij, *Nature (London)* **431**, 159 (2004).
- [43] Y.-X. Liu, L. F. Wei, J. R. Johansson, J. S. Tsai, and F. Nori, *Phys. Rev. B* **76**, 144518 (2007).
- [44] F. Reiter and A. S. Sørensen, *Phys. Rev. A* **85**, 032111 (2012).
- [45] N. V. Vitanov, T. Halfmann, B. W. Shore, and K. Bergmann, *Annu. Rev. Phys. Chem.* **52**, 763 (2001).
- [46] M. A. Nielsen and I. L. Chuang, *Quantum Computation and Quantum Information* (Cambridge University Press, Cambridge, UK, 2000).
- [47] P. E. Barclay, C. Santori, K.-M. Fu, R. G. Beausoleil, and O. Painter, *Opt. Express* **17**, 8081 (2009).
- [48] D. L. McAuslan, J. J. Longdell, and M. J. Sellars, *Phys. Rev. A* **80**, 062307 (2009).